Ore Geology Reviews 89 (2017) 40–69

Contents lists available at ScienceDirect

Ore Geology Reviews

journal homepage: www.elsevier.com/locate/oregeo

Young ores in old rocks: Proterozoic iron mineralisation in Mesoarchean banded iron formation, northern Pilbara Craton, Australia

Stephen Sheppard [a,*], Bryan Krapež [a,b], Jian-Wei Zi [a], Birger Rasmussen [a], Ian R. Fletcher [a]

[a] Department of Applied Geology, Curtin University, Kent St, Bentley, WA 6102, Australia
[b] College of Earth Sciences, Guilin University of Technology, 12 Jiangan Road, Guilin 541004, China

ARTICLE INFO

Article history:
Received 27 March 2017
Received in revised form 29 May 2017
Accepted 2 June 2017
Available online 6 June 2017

Keywords:
Xenotime
Monazite
SHRIMP geochronology
Pilbara Craton
Iron ore
Mineralisation
Nimingarra Iron Formation

ABSTRACT

The origin of bedded iron-ore deposits developed in greenstone belt-hosted (Algoma-type) banded iron formations of the Archean Pilbara Craton has largely been overlooked during the last three decades. Two of the key problems in studying these deposits are a lack of information about the structural and stratigraphic setting of the ore bodies and an absence of geochronological data from the ores. In this paper, we present geological maps for nearly a dozen former mines in the Shay Gap and Goldsworthy belts on the northeastern margin of the craton, and the first U-Pb geochronology for xenotime intergrown with hematite ore. Iron-ore mineralisation in the studied deposits is controlled by a combination of steeply dipping NE- and SE-trending faults and associated dolerite dykes. Simultaneous dextral oblique-slip movement on SE-trending faults and sinistral normal oblique-slip movement on NE-trending faults during initial ore formation are probably related to E–W extension. Uranium–lead dating of xenotime from the ores using the sensitive high-resolution ion microprobe (SHRIMP) suggests that iron mineralisation was the cumulative result of several Proterozoic hydrothermal events: the first at c. 2250 Ma, followed by others at c. 2180 Ma, c. 1670 Ma and c. 1000 Ma. The cause of the first growth event is not clear but the other age peaks coincide with well-documented episodes of orogenic activity at 2210–2145 Ma, 1680–1620 Ma and 1030–950 Ma along the southern margin of the Pilbara Craton and the Capricorn Orogen farther south. These results suggest that high-grade hematite deposits are a product of protracted episodic reactivation of a structural architecture that developed during the Mesoarchean. The development of hematite mineralisation along major structures in Mesoarchean BIFs after 2250 Ma implies that fluid infiltration and oxidative alteration commenced within 100 myr of the start of the Great Oxidation Event at c. 2350 Ma.

1. Introduction

Bedded iron-ore deposits hosted in banded iron formations (BIFs) of the c. 2630–2445 Ma Hamersley Group (Trendall et al., 2004) have received a great deal of attention for decades (e.g., MacLeod, 1966; Morris, 1980; Martin et al., 1998; Barley et al., 1999; Taylor et al., 2001; Rasmussen et al., 2007a), no doubt because of their economic importance to Australia. Iron ore production in Western Australia (the bulk of which came from the Hamersley Group) escalated from about 233 Mt in 2005/2005 to reach 718 Mt in 2014/2015, which was worth about Au$54.3 billion (http://www.dmp.wa.gov.au/About-Us-Careers/Latest-Statistics-Release-4081.aspx), even following the collapse of iron ore prices early in 2014.

The prized high-grade hematite ores of the Hamersley Group show a strong structural control and preserve evidence for a causal relationship to hydrothermal fluids, recognition of which shifted opinion from earlier supergene models (e.g., Morris, 1985) to hypogene models for the ore (e.g., Taylor et al., 2001). However, in the absence of suitable minerals to date either within the ore or in alteration assemblages, mineralisation has been variously linked to: (1) development of a N-verging, fold-and-thrust belt along the southern margin of the Pilbara Craton during the 2215–2145 Ma Ophthalmia Orogeny (Powell et al., 1999; Taylor et al., 2001), (2) late-orogenic collapse at 2100–2050 Ma following orogeny (Barley et al., 1999) and (3) flood-basalt volcanism and continental extension at c. 2008 Ma (Müller et al., 2005). All three hypotheses are consistent with the presence of pebbles of hematite ore in

* Corresponding author.
E-mail addresses: stephen.sheppard@curtin.edu.au (S. Sheppard), bryan.krapez@bigpond.com (B. Krapež), j.zi@curtin.edu.au (J.-W. Zi), B.Rasmussen@curtin.edu.au (B. Rasmussen), ianfletcher47@bigpond.com (I.R. Fletcher).

http://dx.doi.org/10.1016/j.oregeorev.2017.06.003
0169-1368/

some younger Paleoproterozoic strata (Morris, 1980; Martin et al., 1998).

In one of the archetypal Hamersley hematite deposits, the Mount Whaleback Mine (Fig. 1), the main cleavage that developed during the Ophthalmia Orogeny is defined by sericite in black shale and by platy hematite within the ore body (fig. 58 of Tyler, 1991). Irregular grains of monazite which engulf the sericite and quartz but are aligned with the foliation, yielded an ion microprobe U–Pb age of 2175 ± 35 Ma (Rasmussen et al., 2005). At the Mount Tom Price Mine about 200 km to the WNW of Mount Whaleback, metamorphic monazite in black shale yielded an age of 2216 ± 13 Ma (Rasmussen et al., 2005) whereas xenotime intergrown with hematite ore provided a range of ages from c. 2145 Ma to c. 800 Ma (Rasmussen et al., 2007a). Collectively, these data suggest that ore formation at least began during the Ophthalmia Orogeny.

In contrast to the Hamersley Group, iron mineralisation in the granite-greenstone terrains of the Archean Pilbara Craton has received little attention, with a few exceptions (Brandt, 1966; Podmore, 1990; Waters, 1998). For example, in a paper looking at the timing of hypogene mineralisation in the granite-greenstone terrains, Huston et al. (2002) did not consider iron mineralisation although they acknowledged (p. 733) that "large iron ore deposits are being mined in the northeastern North Pilbara terrain." Angerer et al. (2014) discussed a mineral systems approach to iron ore in Archean and Paleoproterozoic BIF in Western Australia, but did not consider the ores of the northern Pilbara Craton owing to a lack of information on the deposits. However, Duuring et al. (2016) and Teitler et al. (2017) recently investigated several iron deposits in the Pilbara Craton and generated exploration targeting criteria for iron mineralisation. The neglect of the ores hosted in Algoma-type Archean BIF of the craton is somewhat surprising, given that following lifting of Australia's iron ore export embargo in 1961, iron ore at Mount Goldsworthy (Fig. 1) was the first to be developed and exported from the Pilbara in 1966 (Ferguson and Ruddock, 2001). Additionally, some of the largest iron ore deposits in the world are hosted by Algoma-type BIF in greenstone belts of the Carajás mineral province of Brazil (Figueiredo e Silva et al., 2008).

In this paper, we present the results of field mapping and sensitive high-resolution ion microprobe (SHRIMP) U–Pb geochronology of hematite ore bodies from the Archean Shay Gap and Goldsworthy belts in the northeastern part of the Pilbara Craton (Fig. 1). The terms 'high-grade ore' or 'ore' are used to refer to accu-

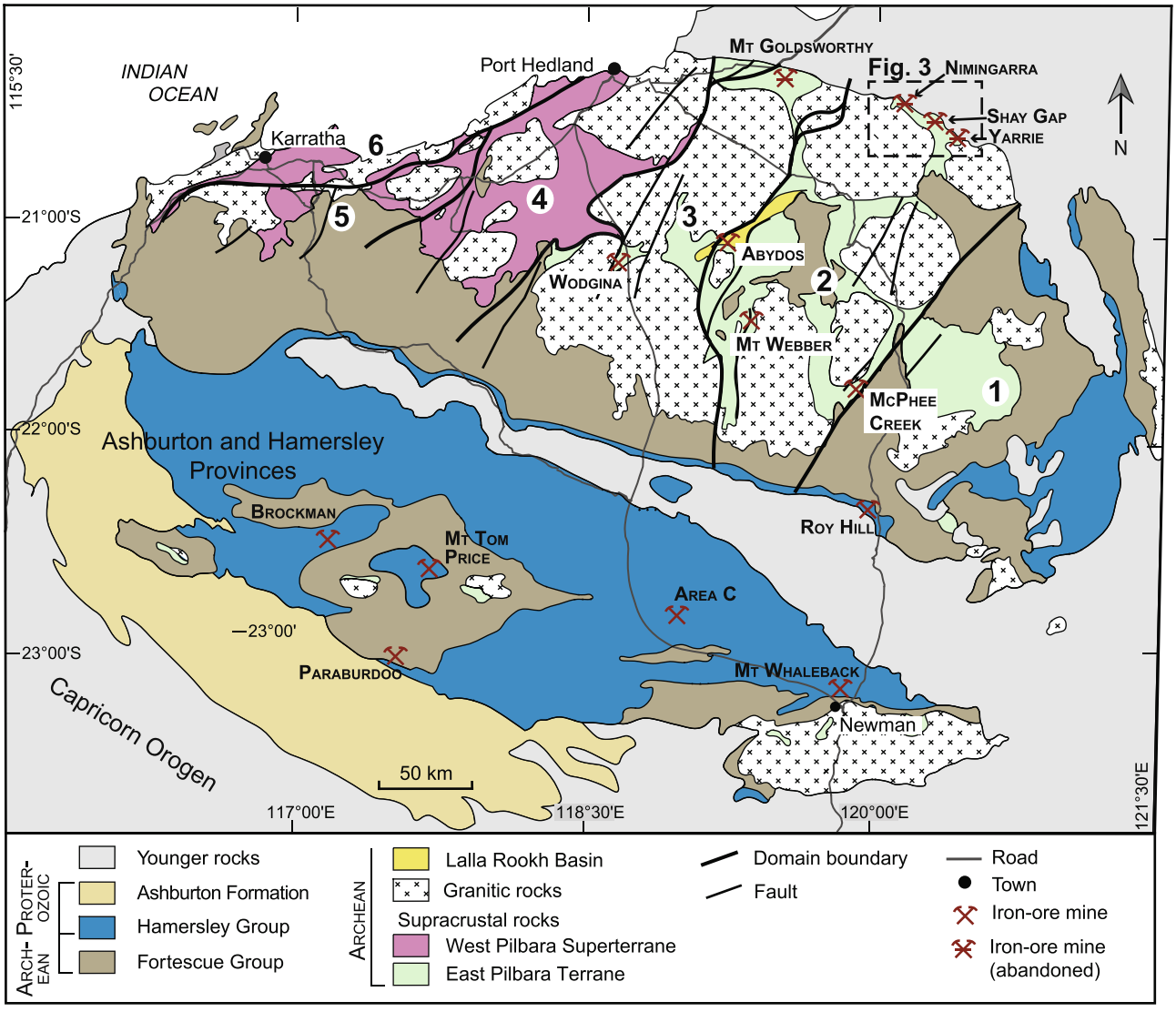

Fig. 1. Simplified map of the Pilbara Craton (modified from Hickman et al., 2010) with pre- to syn-Fortescue Group faults shown; numbers in circles refer to tectonic domains 1–6 from Krapež and Eisenlohr (1998). Location of main faults and boundaries modified from Krapež and Barley (1987), Blake (1993), Krapež (1993) and Krapež and Eisenlohr (1998).

mulations of iron oxides with >55 wt% Fe for consistency with Duuring et al. (2016, p. 22) and to differentiate the ore from low-grade material such as taconite and itabirite. We show that the ores have a strong structural control, particularly by a combination of faults and intersecting dolerite dykes, some of which are strongly mineralised. This work is supported by the first U–Pb SHRIMP dates for xenotime intergrown with hematite from several deposits from Mount Goldsworthy to Yarrie (Fig. 1). A similar geochronological approach has been used on the giant Mount Tom Price ore body in the Hamersley Group (Rasmussen et al., 2007a) and hematite ores from the Marquette Range, Michigan, USA (Rasmussen et al., 2016b).

2. Geology of the Pilbara Craton

The Archean Pilbara Craton comprises numerous supracrustal belts wrapped around oval-shaped granitic complexes (Fig. 1). The craton is composed of a West Pilbara Superterrane (itself a collage of at least three terranes) and an older East Pilbara Terrane, which are interpreted to have been welded together during the Prinsep Orogeny at c. 3070 Ma (Van Kranendonk et al., 2007). Separate depositional basins containing BIFs evolved on the East Pilbara Terrane and the West Pilbara Superterrane. The youngest of these on the East Pilbara Terrane is the extensional c. 3105 Ma Gorge Creek Basin (Sheppard et al., 2017). In contrast, the Cleaverville Basin, a basin with its main stratigraphic component being BIF, developed at ~3020 Ma on the West Pilbara Superterrane (Hickman, 2016).

Following deformation, uplift and erosion of the Gorge Creek and Cleaverville basins, the two-stage, <3020 Ma to >2940 Ma De Grey Basin appears to post-date the stitching together of the East Pilbara Terrane and the West Pilbara Superterrane. The De Grey Basin was defined by Hickman (1990) and revised by Van Kranendonk et al. (2006). Its main components appear to be the Whim Creek, Croydon and Nullagine groups as defined by Van Kranendonk et al. (2006), with the exclusion of the Lalla Rookh Formation. The basin fill, which is nowhere preserved in its entirety, is organised into an initial extensional stage, comprising metasedimentary and metavolcanic rocks, and a later compressional stage, comprising only metasedimentary rocks (Fig. 2).

Following deformation, uplift and erosion of the De Grey Basin during the 2955–2920 Ma North Pilbara Orogeny (Hickman, 2016), a craton-wide array of NE-trending fundamental strike-slip faults developed that split the craton into six tectonic domains (Fig. 1). These strike-slip faults are interpreted to record the attempted tearing apart of the craton in response to a far-field tectonic event (Krapež, 1989; Krapež and Barley, 1987). The Lalla Rookh Formation was deposited in a strike-slip basin (Fig. 1) that developed along the boundary between domains 2 and 3 (Krapež, 1989, 1993; Krapež and Barley, 1987; Eriksson et al., 1994), and is the best evidence of the origin of this late-stage structural architecture.

After cratonisation at c. 2830 Ma, marked by emplacement of the Split Rock Supersuite, the Pilbara Craton was unconformably overlain by siliciclastic sedimentary rock and basalt of the 2775–2630 Ma Fortescue Group (Fig. 1; Blake, 1993; Thorne and Trendall, 2001). Deposition of the lower part of the Fortescue Group was accompanied by normal dip-slip reactivation of the NNE- to ENE-trending basement strike-slip faults (Blake, 1993) and intrusion of NE-trending dolerite dykes of the c. 2772 Ma Black Range Dolerite Suite (Wingate, 1999). Many of the NNE- to ENE-trending Mesoarchean structures therefore have a long history of reactivation, in some instances until at least the Mesoproterozoic (Blake et al., 2011; Sheppard et al., 2016), but even today they are probably the focus of minor earthquakes (Geoscience Australia's Earthquake Database, <http://www.ga.gov.au/earthquakes/searchQuake.do>).

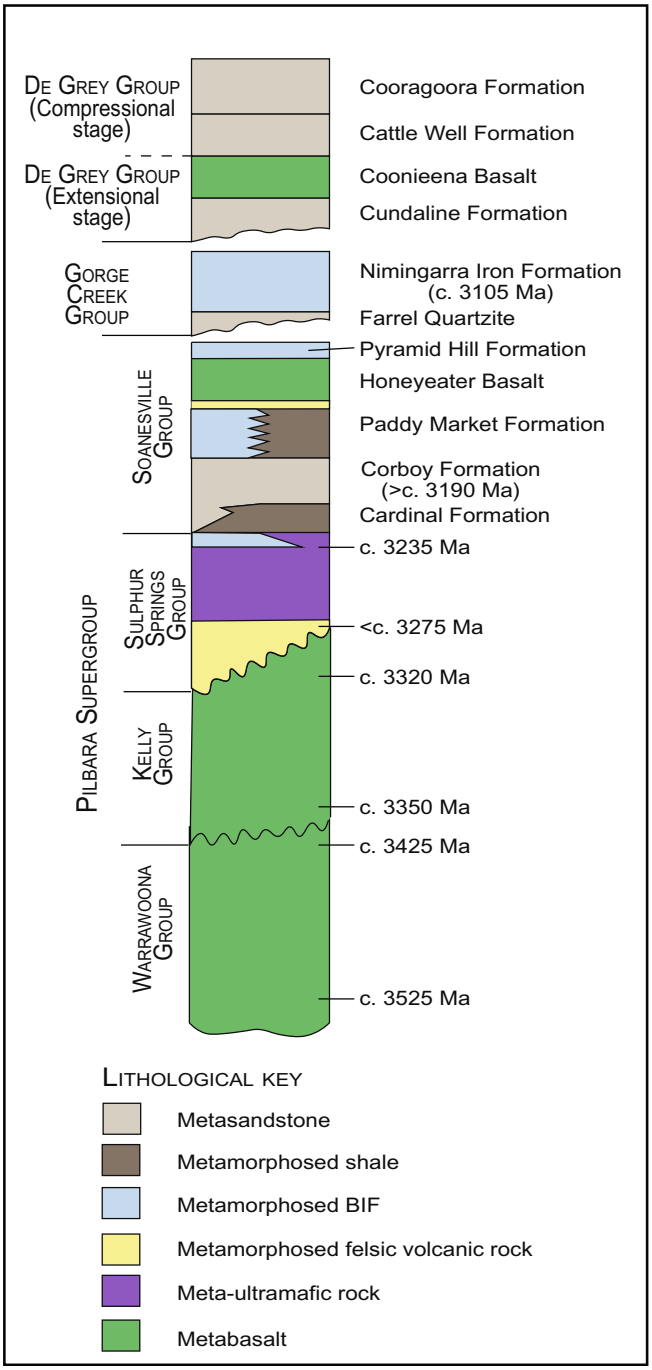

Fig. 2. Generalised stratigraphic column of the Pilbara Supergroup in the East Pilbara Terrane, and the Gorge Creek and De Grey groups in the Shay Gap and Goldsworthy belts (after Sheppard et al., 2017). The lithological key indicates the main rock type present.

Rocks of the Pilbara Craton record a very long history of deformation and metamorphism, and all rocks are metamorphosed at prehnite–pumpellyite to amphibolite facies conditions (Van Kranendonk et al., 2007; Hickman, 2016).

3. Geology of the Shay Gap and Goldsworthy belts

3.1. Overview

The Shay Gap belt (referred to as the 'Shay Gap Belt' by Williams (1999)) comprises rocks of the Gorge Creek and De Grey basins on

the northeastern edge of the Pilbara Craton (Figs. 1 and 2) that nonconformably overlie massive, foliated and gneissic granites of the Muccan and Warrawagine batholiths. The Shay Gap belt forms the northwest-striking limb (Shay Gap to Sunrise Hill) and closure (at Nimingarra) of a large-scale synform (Fig. 3). The dip of bedding rarely exceeds 60° and stratigraphic facing is always upwards. Rocks of the Gorge Creek and De Grey groups in the Goldsworthy belt (Fig. 1) form the southern limb of an ENE-plunging synclinorium cut by the E-trending Goldsworthy Fault. There, the lowest part of the Gorge Creek Group is well-developed and unconformably overlies undivided rocks of the c. 3525–3420 Ma Warrawoona Group (Fig. 2). Both belts contain a unit of BIF estimated to be between 400 and 1000 m thick (Williams, 2003).

In the Shay Gap belt, Dawes et al. (1995a, 1995b) used the name Cleaverville Formation for this BIF with some reservation, because of both the distance between their study area and the type area (>300 km) at Cleaverville (Fig. 1), and the possible presence of tectonostratigraphic terranes within the craton (e.g., Krapež, 1993). This caution was followed by Williams (1999, 2000, 2003) and Smithies (2004), who mapped the Shay Gap and Goldsworthy belts, for the same reasons. These authors opted against using the name Cleaverville Formation, since a correlation with the type area had not been proven and, instead, chose to use a local name: the Nimingarra Iron Formation. Subsequently, Van Kranendonk et al. (2006) applied the name Cleaverville Formation to rocks formerly assigned to the Nimingarra Iron Formation, and abandoned the latter name because it was decided there was only one horizon of BIF. However, recent dating of a tuff unit from within the formation in the Shay Gap belt at 3104 ± 16 Ma (Sheppard et al., 2017), indicates that this BIF does not belong to the c. 3020 Ma Cleaverville Formation. Therefore, in this paper we use the name Nimingarra Iron Formation for the BIF of the Shay Gap and Goldsworthy belts.

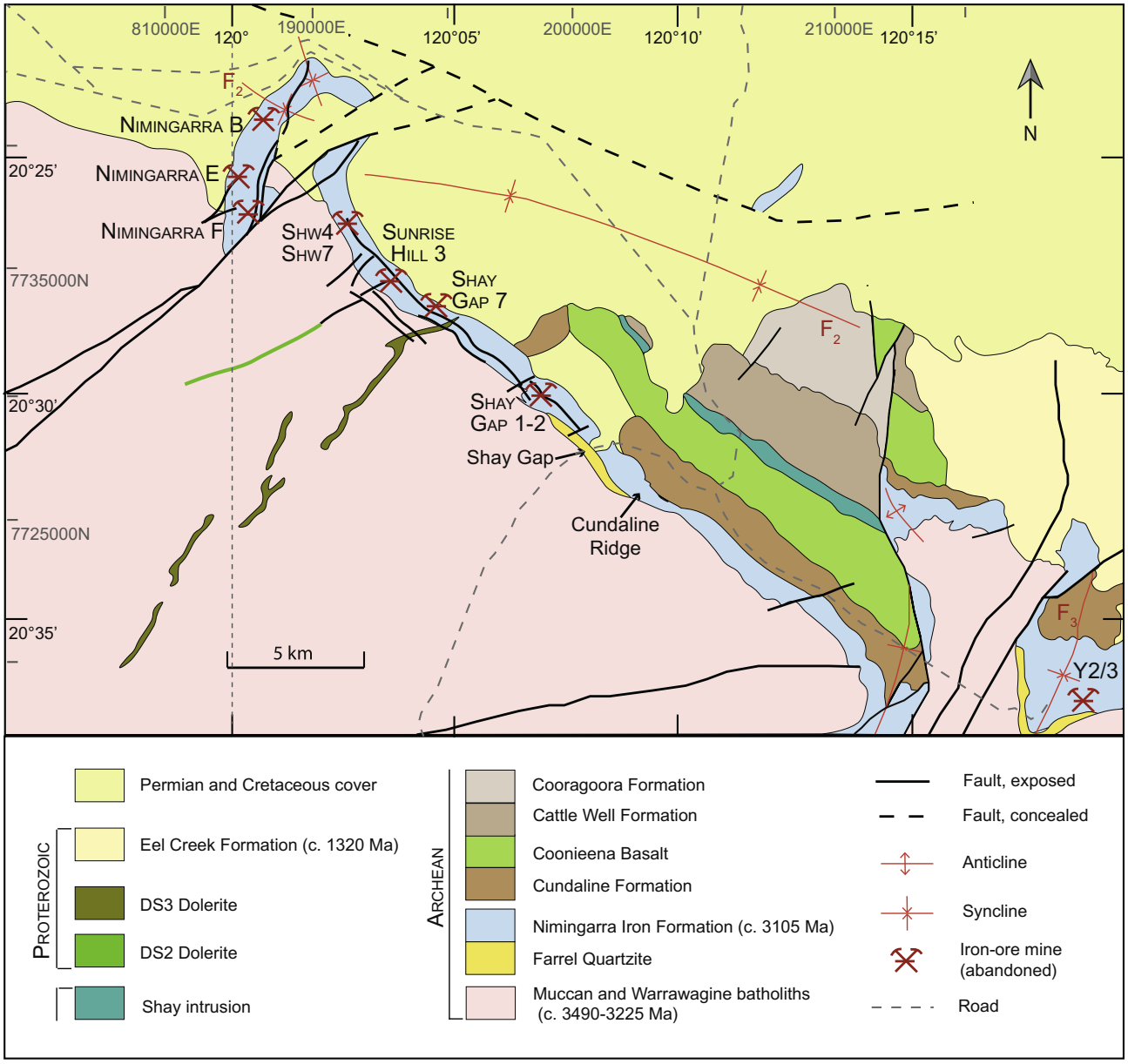

Fig. 3. Interpreted geology of the Shay Gap belt showing the locations of iron-ore mines. Coordinates are shown in both latitude/longitude and UTM systems as the map includes an MGA94 zone boundary. Geology modified from GSWA's 1:500,000 Interpreted Bedrock Geology, 2016 layer (http://geodownloads.dmp.wa.gov.au/datacentre/datacentreDb.asp) based on our mapping; topographic information from the 1:250,000 Topographic Mosaic layer in GSWA's interactive geological map (https://geoview.dmp.wa.gov.au/GeoViews/?Viewer = GeoVIEW).

3.2. Gorge Creek and De Grey groups

Rocks of the Gorge Creek Group (Dawes et al., 1995a,b; Williams, 1999; Bühler, 2008; Sheppard et al., 2017) were originally defined as comprising three formations (Hickman, 2016): namely, from oldest to youngest, the Farrel Quartzite, Nimingarra Iron Formation and Cundaline Formation (Fig. 2). All rocks of the Gorge Creek Group have been metamorphosed, although typically at low grade, and sedimentary and igneous structures are commonly well preserved. For the sake of brevity and clarity, the prefixes 'meta' and 'metamorphosed' are not used for individual rock names, although metamorphism is implied.

The base of the Gorge Creek Group consists of plane-bedded and trough cross-bedded, medium-grained quartzose sandstone, quartzolithic boulder, cobble and pebble conglomerate, and green mudrock. This unit is present everywhere, but is often only ~1 m thick. In the Nimingarra area, this basal unit is up to 30 m thick, and is dominantly trough cross-bedded sandstone. The basal unit was previously included in the Nimingarra Iron Formation (Dawes et al., 1995a,b; Williams, 1999), but Bühler (2008) and Sheppard et al. (2017) regarded these siliciclastic rocks to be the basal section of the Farrel Quartzite (Fig. 2), because the unit gradually expands in thickness to the WNW, SW and south to become recognisable Farrel Quartzite.

The Nimingarra Iron Formation (Fig. 2) in the area SE of Shay Gap has been described in some detail by Bühler (2008), who subdivided it into a 'Lower Member', 'Middle Member' and 'Upper Member'. Sheppard et al. (2017) recognised the same subdivision over the Mount Goldsworthy–Shay Gap–Yarrie area, but referred to the units as the lower BIF member, middle mudstone member, and upper BIF member to reflect the informal nature of the subdivision. The base of the formation in the area is defined as the lowermost Fe-rich band in banded chert (Bühler, 2008).

The lower BIF member is made up of jaspilitic BIF with rare interbedded chert. Siliciclastic sedimentary rocks of the middle mudstone member, which overlie the BIF on an erosion surface, are a fining upwards sequence of medium-grained massive and graded sandstone (turbidites), laminated mudrock, pyritic black shale and chert. The unit is up to 70 m thick in the Sunrise 7 pit, but is commonly structurally attenuated by strike-parallel faults. A thin tuff bed from the middle mudstone member in the Sunrise West 8 pit is dated at 3104 ± 16 Ma (Sheppard et al., 2017). The contact of the middle mudstone member with the overlying upper BIF member is conformable. The upper BIF member is similar to the lower, comprising jaspilitic BIF with rare interbedded early diagenetic, laminated chert.

The Nimingarra Iron Formation in the Nimingarra–Yarrie area is unconformably overlain by deltaic sandstone and shale of the Cundaline Formation (Fig. 2; Williams, 2003; Bühler, 2008; Sheppard et al., 2017). The unconformable relationship negates its assignment to the Gorge Creek Group; rather, the Cundaline Formation is the basal unit of the De Grey Group. The Cundaline Formation in the Shay Gap belt is conformably overlain by basalt, basaltic hyaloclastite and subvolcanic dolerite sills of the Coonieena Basalt, which together identify the extensional stage of the De Grey Basin (Fig. 2). The succession above the Coonieena Basalt, namely the Cattle Well and Cooragoora formations (Fig. 2), is also conformable and records a shallowing upwards from deep-marine basinal shale through delta-front sandstone and shale to delta-top (fluvial) sandstone (Bühler, 2008). The combined Cattle Well and Cooragoora formations define the compressional stage of the De Grey Basin.

In the Mount Goldsworthy area, the Nimingarra Iron Formation is unconformably overlain by a sequence of quartzolithic sandstone which is referred to as the Paradise Plains Formation (Smithies, 2004), and therefore is also part of the De Grey Group. In the core of the Goldsworthy Synclinorium, that sandstone sequence is conformably overlain by basalt, some of which preserves spinifex textures. These siliciclastic sedimentary and mafic volcanic rocks, therefore, have an identical stratigraphic position to the lower part of the De Grey Group in the Nimingarra–Yarrie area.

3.3. Dolerite dykes

There are three obvious sets of dolerite dykes, plus a possible fourth, older set, and a fifth, younger set. The oldest set (DS1), which comprises mafic and ultramafic compositions, crops out only in the northwest sector of Sunrise Hill, where it strikes roughly E-SE, but is clearly dislocated by a NW-trending fault set. A second set of dykes (DS2; Fig. 3) trends approximately NE and N, can be tracked through the Muccan batholith, and is offset dextrally by NW-trending faults. This set of dykes is commonly altered to iron oxide minerals on its bounding surfaces, but in some places is totally replaced by iron ore. DS2 dykes are easily identified where they cross BIF, but are difficult to trace through granite because they do not have a positive topographic expression. The third set of dykes (DS3; Fig. 3) is the c. 2772 Ma Black Range Dolerite Suite, which was a feeder to the Fortescue flood basalts (Lewis et al., 1975; Hickman, 1983; Wingate, 1999), and which can easily be identified on aerial photographs and satellite imagery because of the great strike length of individual dykes. The fourth set of dykes (DS4) is genetically associated with small-scale fault arrays, typically replacing or smearing along fault planes, or developed in swales in fault planes. The dykes are commonly totally replaced by iron oxides, and in some iron-ore pits may have been the principal host of iron ore. They vary from well-defined strike-persistent structures, to chaotically oriented structures with fluidal margins, and range in width from several metres down to a few centimetres. DS4 dykes are typically highly altered, and can be replaced by iron-ore even where they intrude the granitic basement. At Mount Goldsworthy mine (Fig. 1) a dolerite dyke that cuts through ore and the bounding structure is clearly the youngest dyke generation, and for those reasons is referred to as DS5.

3.4. Mesoproterozoic sedimentary rocks

At the SE end of the Shay Gap belt, Archean granitic and supracrustal rocks are nonconformably and unconformably overlain by siliciclastic sedimentary rocks of the Eel Creek Formation (Fig. 2; Williams, 1999, 2003). Two tuff samples from near the base of the succession have been dated at 1318 ± 7 Ma and 1310 ± 8 Ma (Sheppard et al., 2017).

3.5. Permian, Mesozoic and Cenozoic units

East and SE of the Shay Gap deposits, Archean rocks are overlain by poorly exposed Permian fluvioglacial rocks that occupy a narrow valley that is "marginal to the Canning Basin, which is the main depocentre of Permian rocks in the region" (Williams, 1999; p. 27). All Precambrian rocks in the Shay Gap region are overlain unconformably by widespread Late Cretaceous–Early Jurassic siliciclastic rocks of the Callawa Formation, which are preserved in a series of scattered buttes and mesas (Williams, 1999). In the Shay Gap area these Late Cretaceous–Early Jurassic rocks comprise fluvial conglomerate and trough cross-bedded sandstone. Various Cenozoic sedimentary rocks overlie all other sequences, and include alluvial-fan conglomerate and cemented colluvium, which commonly contain pebbles of hematite ore.

4. Structure of the Shay Gap belt

The Shay Gap belt forms the NW-striking, southwestern limb (Shay Gap-Sunrise Hill) of a large-scale F_2 synform, and the northwestern closure (at Nimingarra) of that synform (Fig. 3). Stratal dips rarely exceed 60°, and stratigraphic facing is always upwards. A NW-trending, near-vertical cleavage is weakly developed parallel to the axial surface of the synform. There are numerous small-scale parasitic folds (F_2) that plunge to the SE, complementing the synform. There are also small folds that plunge to the NE (F_3), and which are related to the cross folding that produced the large-scale basinal structure. There are also chaotically oriented intrafolial folds (F_1). Around Yarrie, the Archean supracrustal rocks dip NE through to NW and mostly appear to face north, but are folded into a basinal structure in which the northern limb has been removed below the unconformity at the base of the Mesoproterozoic Eel Creek Formation. There are a number of generally N- to NE-trending, simple open folds. The F_1 through to F_3 folds are all cut by the c. 2772 Ma DS3 dolerite dykes.

More significant with regards to iron-ore generation is a set of NE-trending faults (Fig. 3). The faults have steep dips to either the NW or SE and define NE-trending horsts and gräben. The faults vary in displacement from ~5 km (e.g., the fault that separates the Sunrise Hill line from the Nimingarra line; Fig. 3), to faults with only a few metres dislocation. These faults follow the trend of the Archean set of fundamental structures. The fault array can be linked genetically to DS4 dolerite dykes and iron ore. Where vectors can be determined, this set of faults has a sinistral sense of dislocation. A complementary set of faults strikes SE, and is well developed in the Shay Gap–Sunrise Hill line (Fig. 3). The faults are best seen within the Muccan batholith, where they offset a NE-trending DS3 dolerite dyke, giving an apparent clockwise rotation in the strike of that dyke into the Nimingarra Iron Formation. Those faults trend back into Sunrise Hill, where several are spatially related to iron-ore. Faults have a dextral sense of dislocation, but there are also chaotic sinistral offsets. They are steeply dipping, either to the NE or to the SW, and in pairs can also develop horsts and gräben. DS4 dolerite dykes are genetically linked to these faults.

The NE-trending sinistral faults and complementary SE-trending dextral faults are consistent with either a regional E-W extensional stress regime or a regional N-S compressive stress regime that was younger than the c. 2772 Ma DS3 dolerites. Fault-hosted DS4 dolerite dykes and the absence of regional folds of the same age imply the tectonic regime was extensional.

5. Descriptions of hematite ore-bodies

5.1. Background

Iron ore mining began in the Shay Gap belt in 1972 to supplement production from Mount Goldsworthy. By 1993 the town of Shay Gap, and the mines around it, had been shut down with production replaced by the Yarrie deposits to the SE. In 1997, production from Yarrie was supplemented by the ores from the Nimingarra area. Currently all mines in the Shay Gap belt either have been exhausted or placed under care and maintenance.

The area examined here includes, from SE to NW, the Yarrie, Cundaline Ridge, Sunrise Hill, Shay Gap, Nimingarra and Mount Goldsworthy deposits (Fig. 1). Iron mineralisation is developed over much of the 25 km strike length of the Nimingarra Iron Formation in the area. Twenty iron ore pits, providing varying degrees of access, were mapped as part of the project. Where pits were filled or partly filled with water, mapping was conducted around the pits and on any accessible pit faces or the walls of access ramps. The names used for the pits are from the Mines and Mineral Deposits (MINEDEX) database of the Geological Survey of Western Australia (http://minedexext.dmp.wa.gov.au/minedex/external/common/appMain.jsp). Of the roughly two dozen pits examined, geological maps are presented here for 11 of them; the following discussion will concentrate on those deposits as they provided the most information. Iron mineralisation mainly comprises hematite-martite(-magnetite), with hematite consisting of both microplaty and coarser grained crystals. At least minor goethite is present in all samples, but it increases in abundance in concert with the degree of weathering.

5.2. Yarrie (Y2/3)

Although there is little detail preserved on the plunge of the Y2/3 ore body, it was fault bounded and developed mostly, but not exclusively, in BIF of the lower member of the Nimingarra Iron Formation (Fig. 4). Ore is preserved only along the trace of a curved fault complex that today outlines the northern wall of the pit. This fault complex is a flower structure that includes a sliver of basement granite and Farrel Quartzite (Fig. 4). There is also a DS4 dolerite dyke, which has an irregular trace along the northern wall, and juxtaposes BIF to the north and chloritised basement granite to the south. The dolerite intrudes the fault for its entire trace, and can also be seen within a NW-trending fault to the south of the mine.

The apparent repetition of folded basement and the Farrel Quartzite within the pit (Fig. 4) is a consequence of the three-dimensional exposure. Although the ore is fault bounded on its northern side, the structural setting of the ore is a gräben between

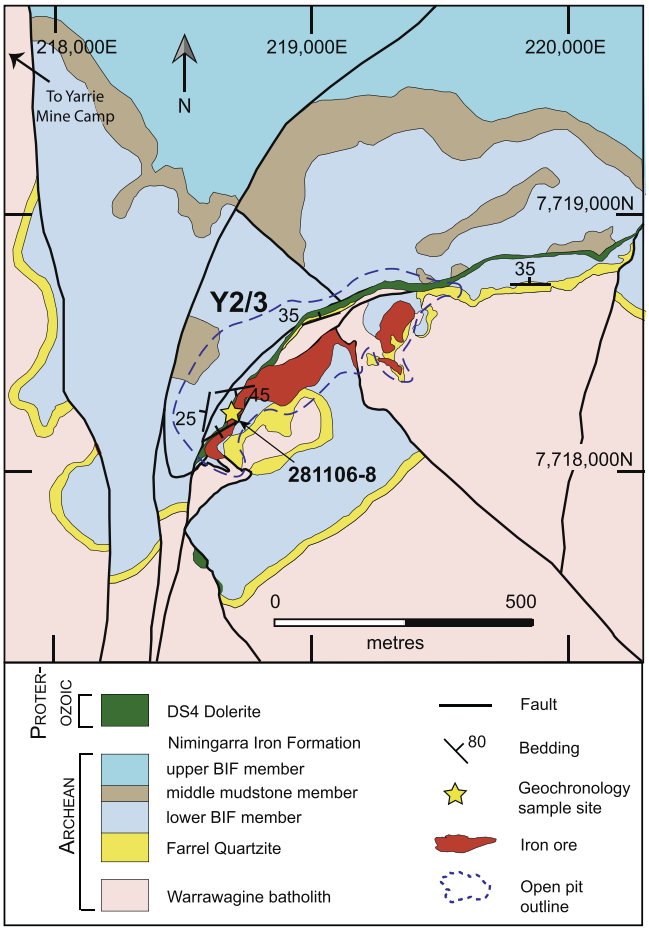

Fig. 4. Solid geology map of the Y2/3 ore body at Yarrie.

NW-trending normal faults (Fig. 4). Those NW-trending faults reappear on the northern side of the northern-wall fault, with only minor dextral offset, but they do not pass through the internal flower structure. The western wall of the pit is granite on the western side of the fault plane; the irregular trace of the bounding fault on the map (Fig. 4) is due to the three-dimensional exposure. High-grade iron-ore is not developed solely in BIF within the Y2/3 pit; rather, DS4 dolerite in the fault is mineralised (Fig. 5A), and in places is entirely replaced by iron oxides. Ore development appears to be chaotic, with lozenges of un-mineralised dolerite. However, there is no ore in the northern-wall section of the dolerite within the flower structure.

The structural setting of ore formation therefore includes three elements: (i) iron-rich host rocks, namely banded iron formation and DS4 dolerite; (ii) laterally limiting structures, namely normal dip-slip faults that define a graben structure; and (iii) the controlling strike fault (Fig. 4). Ore appears to have plunged down the intersection of primary layering and the NW-boundary fault, implying that the fault was the fluid conduit. Kinematic indicators on the controlling fault are not preserved, but in the ore position the flower structure appears to occupy a right-handed bend, which obviously enhanced both the intrusion of the DS4 dolerite and ore formation. The chlorite alteration within the flower structure is a feature common to all DS4 dykes.

5.3. Shay Gap 1–2

Along strike to the SE from Shay Gap 1–2, the lower BIF member of the Nimingarra Iron Formation is faulted down to the NE against granitic basement (Fig. 6). That NE-dipping, SE-striking fault continues along strike into the pit, where it forms the upper surface of the middle mudstone member, and the lower bounding surface to the ore body (Fig. 6). A NW-trending DS4 dyke has intruded the lower bounding fault and is locally mineralised. There is a multitude of even smaller DS4 dykes, many only tens of centimetres wide, with fluidal contacts, and with the same strike as the two sets of faults: namely, SE trending and NE trending.

No iron ore is preserved within the pit, which is deeply flooded. From the shape of the pit, it appears that ore sat on the hanging-wall of the SE-striking fault, and most likely plunged to the SE down the intersection of the fault with primary layering in the upper BIF member of the Nimingarra Iron Formation. There is a spatial association with the middle mudstone member, but the association is structural rather than stratigraphic. At least some of the ore appears to have been mined from dolerite. The structural setting of the ore body therefore appears to have three elements: (i) iron-rich host rocks, namely banded iron formation and DS4 dolerite; (ii) laterally limiting structures, namely a NNW-trending

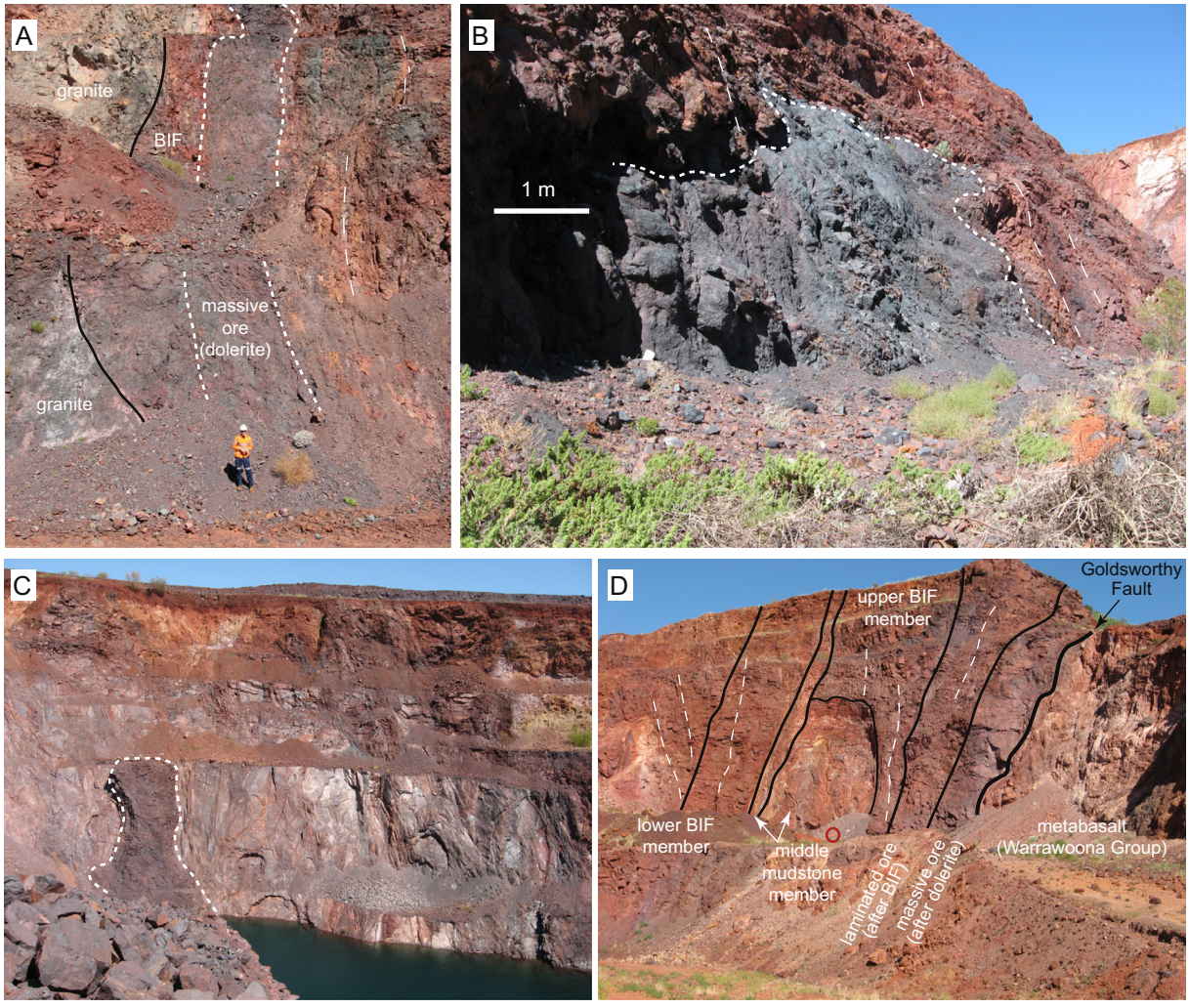

Fig. 5. A) Mineralised dolerite in the northern wall of the Y2/3 pit (at approximately MGA94 Zone 51 188250E 7741350N). B) Plunging remnant of grey, laminated iron-ore in Shay Gap 7 (at MGA94 Zone 51 194750E 7733655N). Note discordance of ore to primary layering in BIF. C) Remnant of iron-ore (outlined) adhering to the fault plane in the Nimingarra B pit. D) Fault-bounded, mineralised BIF and shale in the Goldsworthy pit. Looking west. Person in small red circle for scale.

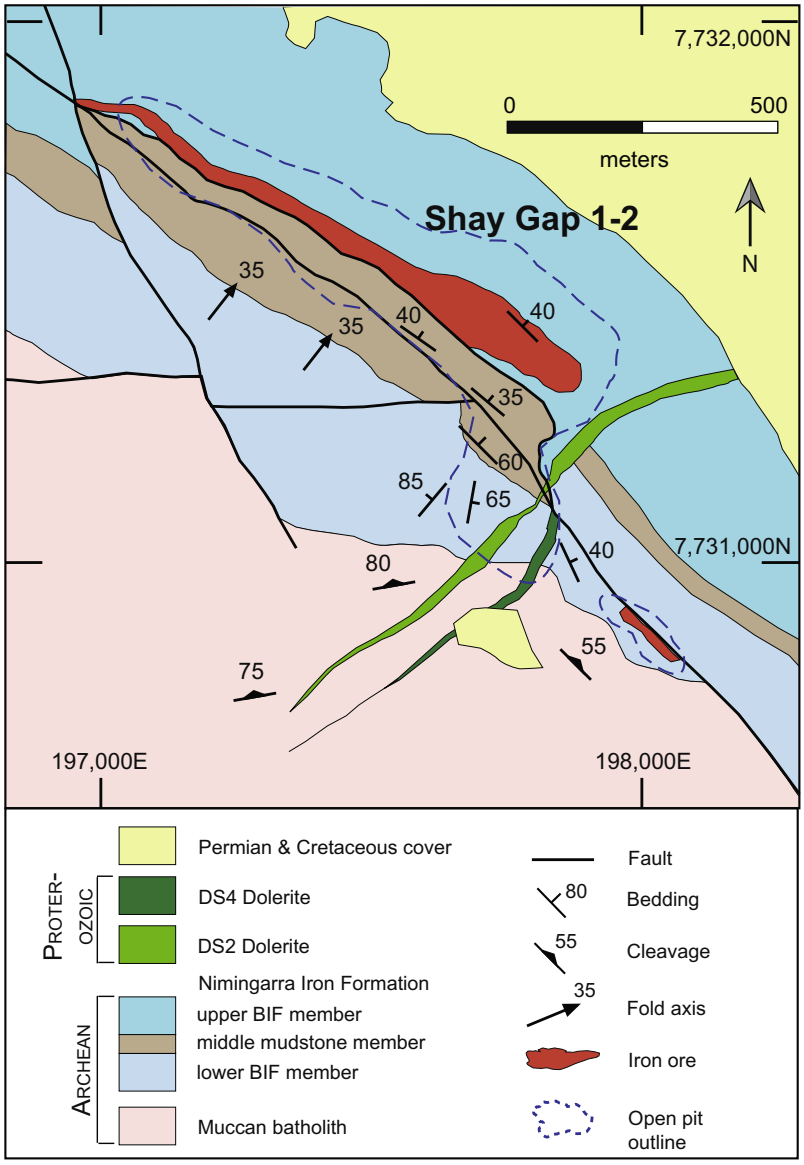

Fig. 6. Solid geology map of the Shay Gap 1–2 ore bodies. Coordinates are Map Grid of Australia 94, Zone 51.

fault on the northwestern boundary and a DS2 dolerite on the southeastern boundary; and (iii) a controlling strike fault (Fig. 6).

5.4. Shay Gap 7

Iron ore is preserved just above the water line near the eastern margin of the Shay Gap 7 pit. Its northwestern wall, and the approximate limit of ore, is a NE-trending, faulted DS2 dolerite dyke (Fig. 7) the outer metre or less of which is mineralised. Numerous DS4 dykes are parallel to, and intrude, SE-trending faults. Those dykes are all mineralised, and in places are totally replaced by iron ore. The northeastern margin of the pit comprises Cretaceous rocks, whereas thin-bedded turbidites and shales of the Cundaline Formation are exposed along the northwestern wall, and identify a parasitic F_2 fold. The DS2 dolerite dyke cuts across that parasitic fold. The south wall comprises steeply dipping, folded shale of the middle mudstone member, overlying folded BIF. The upper contact of the middle mudstone member is marked by a fault-hosted DS4 dolerite (Fig. 7) in which high-grade iron ore is preserved in situ. Massive ore, therefore, appears to have been developed on bounding DS2 and DS4 dolerite dykes, but the principal lode plunges steeply to the E, and is developed in BIF. Laminated ore is preserved (Fig. 5B), as too is an outer carapace of brecciated ore that plunges concordantly with the laminated ore. The plunging remnant of ore clearly illustrates that its outer limits cut across primary layering.

In the Shay Gap 7 deposit it appears that ore plunged in the direction defined by the intersection between a footwall bounding, NE-dipping and SE-trending fault/DS4 dolerite and bedding in the BIF. Although there is an apparent lithological control on ore (ore being developed along the contact between the middle mudstone member and overlying BIF), the contact is a fault, and it is that fault which is the controlling structure. The DS2 dyke was the limiting structure to the NW, but no limiting structure is preserved to the SE.

5.5. Sunrise Hill 3

Sunrise Hill 3 consists of several abandoned pits in an area of complex geology resulting from the dismemberment of the NW-

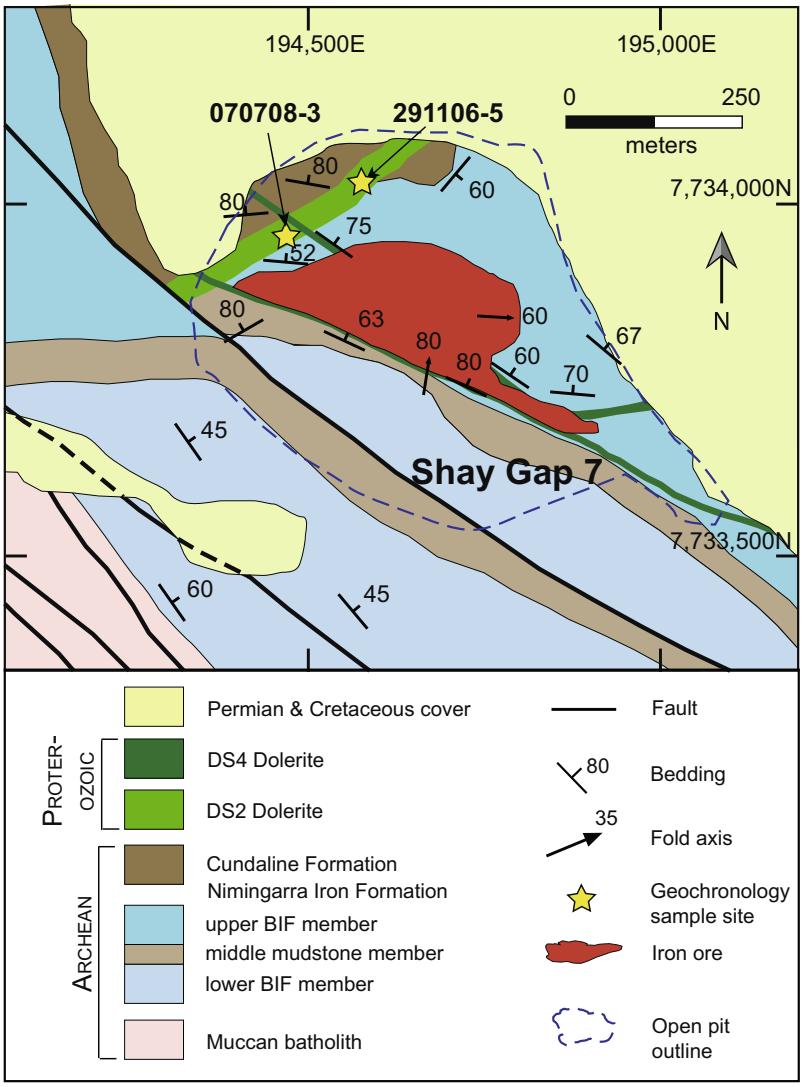

Fig. 7. Solid geology map of the Shay Gap 7 ore body. Coordinates are Map Grid of Australia 94, Zone 51.

striking strata by NE-trending sinistral and SE-trending dextral faults (Fig. 8). The DS2 dolerite dyke from SH7 is repeated here, dislocated dextrally, and there are also several other dolerite dykes of the same age. Those DS2 dykes are demonstrably truncated to the SW by a dextral strike-slip fault, and juxtaposed against granite. However, there is also a series of DS4 dolerite dykes intruding the two principal fault trends. As with the Shay Gap pits, the DS4 dykes often have fluidal boundaries and host iron ore. Not all ore is spatially associated with the middle mudstone member, but all ore is associated with faults and syn-faulting DS4 dolerite dykes. The principal ore zones appear to be developed in compartments bounded by the two main fault trends.

5.6. SHW4 (southern pit) and SHW7 (northern pit)

In the SHW4 pit, iron ore is developed in the lower BIF member of the Nimingarra Iron Formation (Fig. 9). The ore body, some of which remains, is clearly fault bounded as it lies in the hangingwall of a NE-dipping, SE-striking fault that juxtaposes BIF against basement granite. Ore zones plunge shallowly along the near-parallel intersection of primary layering with the fault plane. There is an abundance of cross-faulting, but most of those faults have more easterly trends, and predominantly normal rather than strike-slip dislocations. This part of Sunrise Hill may be a horst. A thick DS1 dolerite dyke within the pit is truncated by the ore-bounding fault (Fig. 9). DS4 dolerite dykes cut the ore-controlling faults (Fig. 9), but there is no mineralised dyke in SHW4.

At SHW7 it appears that three ore bodies were mined (Fig. 9), with one ore body continuing south into SHW4. There is clearly a fault-offset of the middle mudstone member within SHW7 (Fig. 9), so that a crossing fault must have controlled ore geometry. However, remnants of ore on both the SE and NW sides appear to be bounded by parallel, SE-trending faults that dip in opposing directions. Partially mineralised DS4 dolerite bounds remnants of ore. Deposit SHW7 exposes the best section of the middle mudstone member, which is almost 70 m thick. The member is extensively ferruginised, but it is not structurally attenuated on its upper or lower surfaces and, therefore, not a controlling factor in ore genesis.

5.7. Nimingarra F and Nimingarra F (east)

The western pit (Nimingarra F; Fig. 10) is shallow, and there is scant evidence of the shape of the ore body that was mined. Mining appears to have focused on ground immediately above the middle mudstone member but there is no evidence that the contact was a

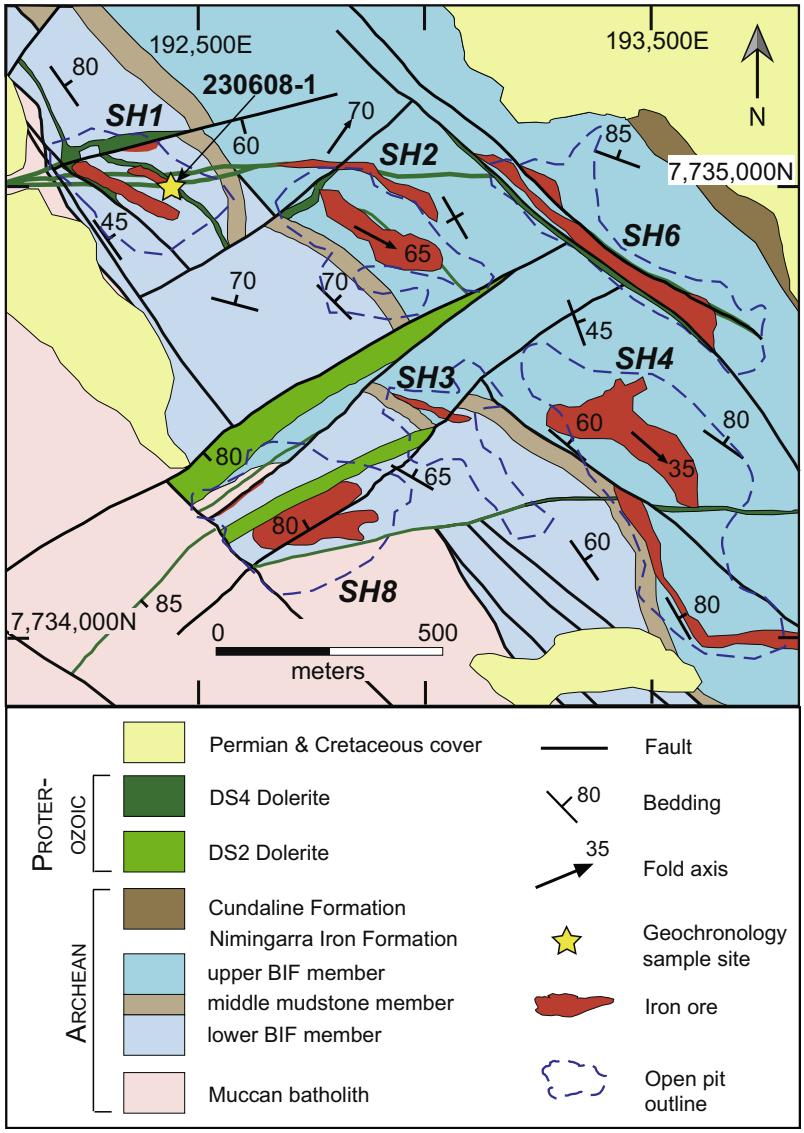

Fig. 8. Solid geology map of the Sunrise Hill 3 ore bodies. Coordinates are Map Grid of Australia 94, Zone 51.

fault. Rather, the middle mudstone member is fully developed with thick beds of unaltered sandstone. This contrasts considerably with the extensive, ore-related ferruginisation seen in the same sandstone bodies in SHW7. There are abundant E- through to NE-trending DS4 dolerite dykes in this sector but none is associated with ore, although they all appear to pre-date ore. The key interpretations from Nimingarra F pit are that: (1) a coincidence of faults and fault-hosted DS4 dolerite was required to set up preferred fluid conduits for mineralisation, and (2) once again a lithological contrast between BIF and siliciclastic sedimentary rocks of the middle mudstone member is a misleading exploration model because ore zones require favourable structural relationships between faults, dykes and primary layering in BIF.

In contrast to Nimingarra F pit, the eastern pit (Nimingarra F East) has a demonstrable relationship with structure-hosted DS4 dolerite, and the ore body appears to have plunged steeply to the southeast (Fig. 10). High-grade specular hematite was mined from this pit, although no ore can be seen in situ.

5.8. Nimingarra E

Nimingarra E consisted of two narrow ore bodies that are fault bounded and associated with fault-hosted DS4 dolerite (Fig. 11). The eastern ore body comprises both mineralised BIF and dolerite. In both ore bodies the controlling faults and included dolerite dykes dip to the SE. Ore in the western deposit is developed in the lower BIF member of the Nimingarra Iron Formation, whereas the eastern deposit is developed along the fault and in dolerite immediately above the fault-attenuated middle mudstone member. In the northern part of the pit, the eastern ore body follows the trace of the fault and dolerite, breaking out of the contact with the middle mudstone member into the upper member of the Nimingarra Iron Formation. This is an excellent example showing that the lithological contrast between the middle mudstone member and the upper or lower BIF members did not control ore formation.

5.9. Nimingarra B

Nimingarra B (Fig. 12) was the largest deposit in this sector, although it is mostly inaccessible and has been partially backfilled. The northwestern boundary of the Nimingarra B pit is a NNE-trending, curved fault with fault-hosted DS4 dolerite dyke separating the middle mudstone member (on the northwest side) from the upper BIF member (on the SE side). The ore appears to have thickened to the southwest, towards a conspicuous bend in the fault

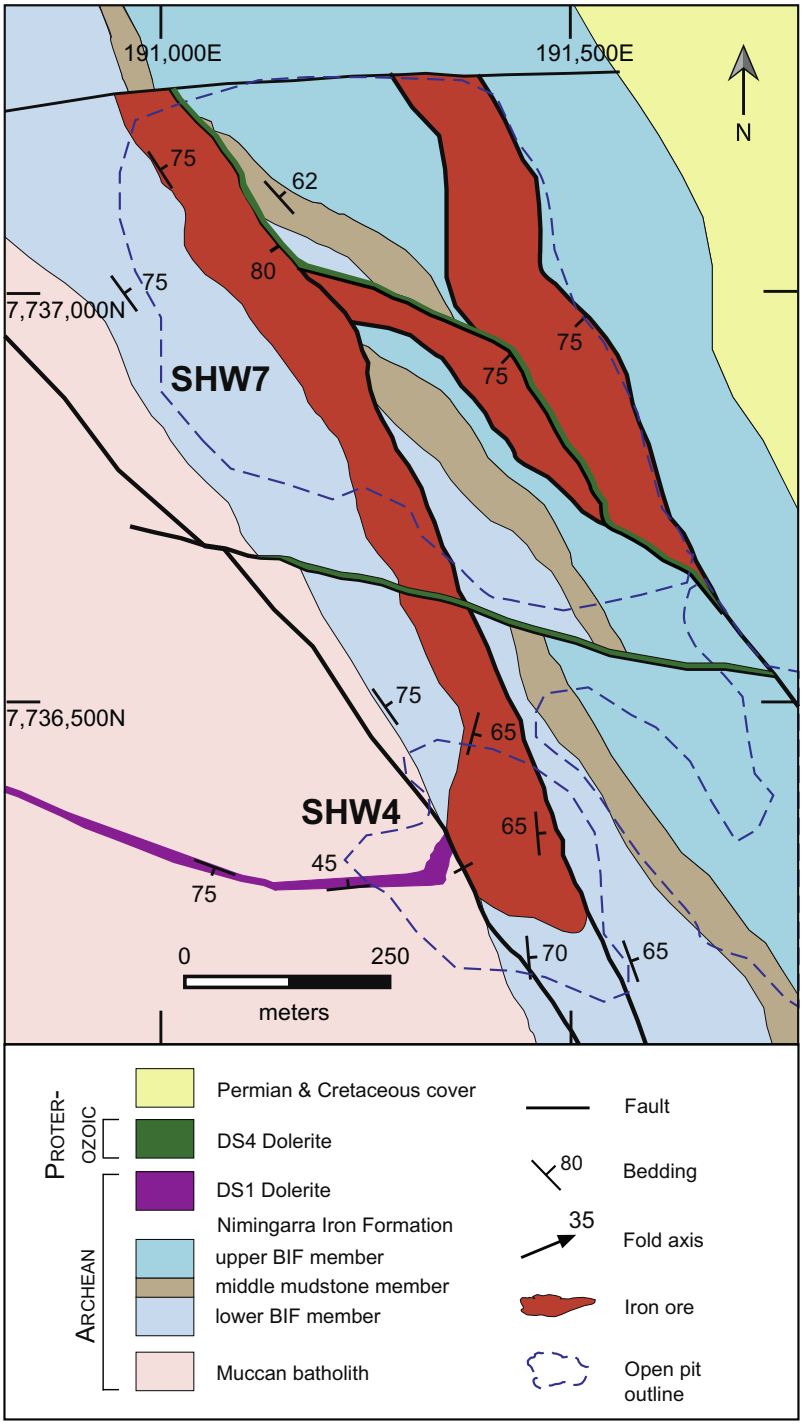

Fig. 9. Solid geology map of the SHW4 and SHW7 ore bodies. Coordinates are Map Grid of Australia 94, Zone 51.

trace (Fig. 12), and almost certainly plunged to the NE, along the intersection of the fault plane with primary layering. Banded iron formation preserved in the southwest corner is isoclinally folded, and plunges steeply to the NE, which is consistent with observations elsewhere that ore bodies are developed on tightly folded BIF. A remnant of massive ore adheres to the fault plane close to the southwestern corner (Fig. 5C). Remnants of that ore can be traced to the southwest as mineralised and then to unmineralised DS4 dolerite, establishing that the precursor to massive ore was dolerite. This is an identical scenario as seen elsewhere: a close association of ore with faults and DS4 dolerite dykes, and mineralisation commonly replacing dolerite abutting mineralised BIF. What is different in this pit is that bends in the fault trace appear to be associated with the limits of the ore body. Although movement vectors on the fault cannot be examined because of the lack of access, NE-trending faults have sinistral oblique-slip dislocation. The shape of the Nimingarra B fault therefore implies ore developed in a releasing bend, and that bend probably enhanced fluid flow in an extensional regime.

5.10. Mount Goldsworthy

The Mount Goldsworthy mine is located on the southern limb of the E–NE-plunging Goldsworthy synclinorium (Fig. 13). Most

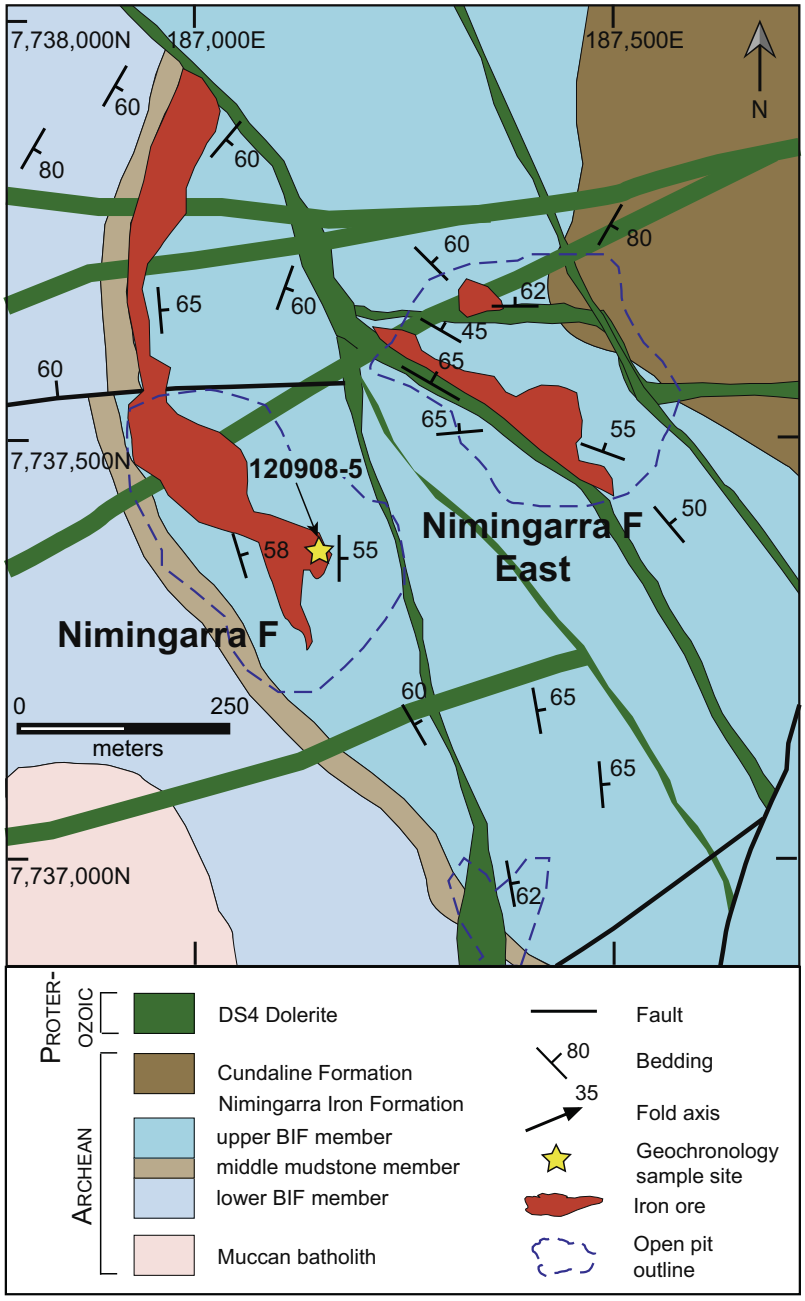

Fig. 10. Solid geology map of the Nimingarra F and Nimingarra F East ore bodies. Coordinates are Map Grid of Australia 94, Zone 51.

faults in the Mount Goldsworthy area are NE trending and SE trending, similar to the orientations seen from Nimingarra through to Yarrie. However, the dominant structure in the Mount Goldsworthy area is the generally E-trending Goldsworthy Fault, along which the mine workings are located (Fig. 13). Although the fault appears to have a large sinistral dislocation, kinematic indicators on the fault plane, which marks the northern wall of the pit, are south-block down, establishing that the latest dislocation on this fault was dip-slip. The fault is close to vertical but varies about 10°, showing apparent reverse and normal movements. Dolerite dykes (DS4) vary in strike from NW to NE, but do not intrude along faults as in the Shay Gap belt. There is an approximately N-trending DS5 dolerite dyke that cuts through ore and the bounding faults (Fig. 13).

The large hematite ore body that was mined at Mount Goldsworthy formed in the nose of a faulted-out syncline in the upper BIF member and is demonstrably fault bounded (Fig. 5D); note that the Nimingarra Iron Formation is slightly overturned along the trace of the Goldsworthy Fault. However, no in situ ore of that ore body is preserved above the waterline, although float material establishes that at least parts of it were high-grade specular hematite. The plunge of the ore body is not obvious from the shape of the pit, but as the fault-bounded folds of the middle mudstone member are upright, the ore body may have plunged subvertically down the plane of the bounding fault. Unlike iron-ore pits from Nimingarra to Yarrie, there is no obvious spatial relationship with DS4 dolerite dykes, and only a coincidental spatial relationship with the middle mudstone member. However, massive ore is preserved at the western limit of the pit, abutting the Goldsworthy Fault (Fig 5D), contrasting markedly to preserved laminated low-grade ore that developed on the upper BIF member. Although original textures are completely obliterated in the mas-

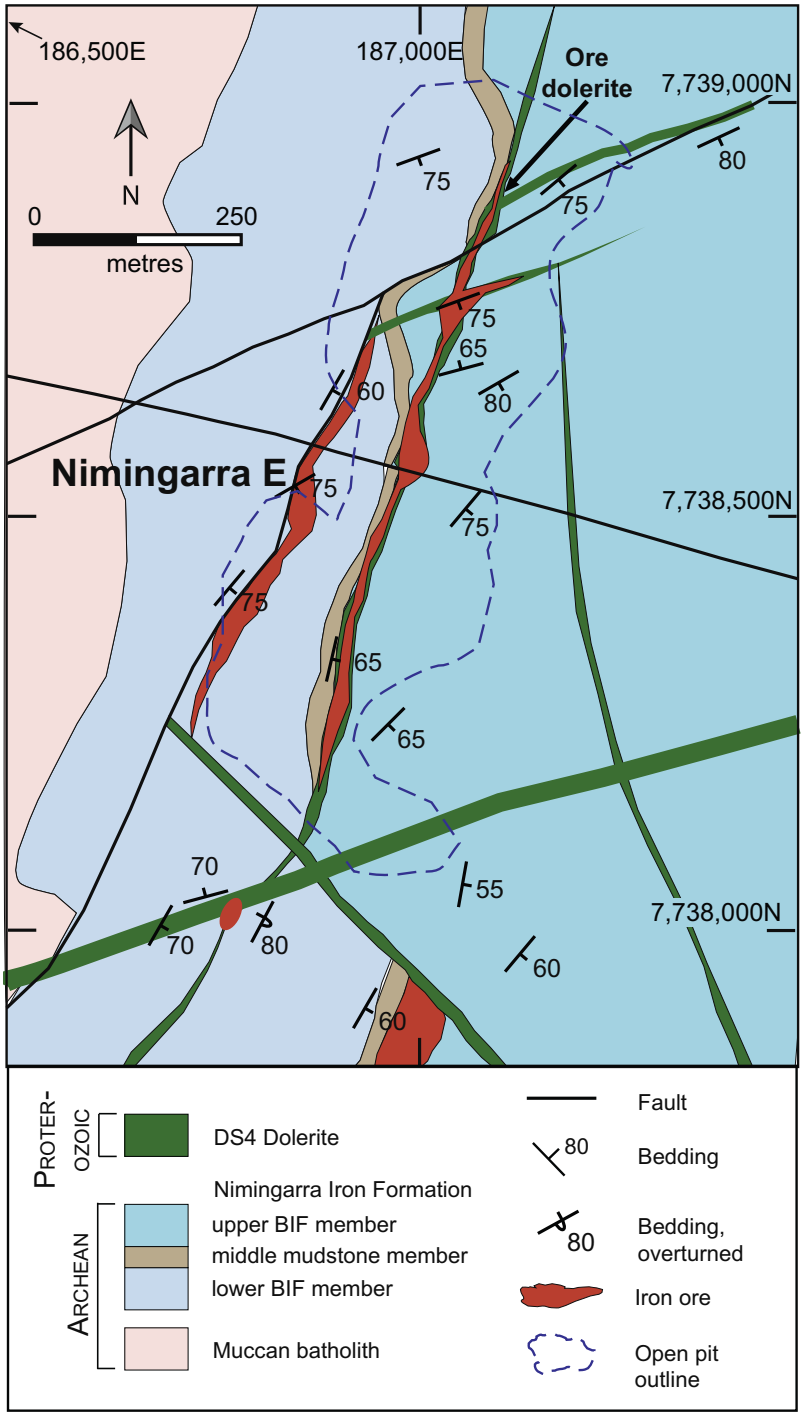

Fig. 11. Solid geology map of the Nimingarra E ore bodies. Coordinates are Map Grid of Australia 94, Zone 51.

sive ore, comparison to the other ore bodies suggests that the precursor to the massive ore was a DS4 dyke, which is consistent with the preserved tabular geometry.

6. Summary of the structural setting of the ore bodies

Iron-ore was developed in structural blocks in which faults and fault-included DS4 dolerite dykes cross at oblique angles, thereby focusing hydrothermal fluids (Fig. 14). Fault bends appear to have focused fluid alteration in an extensional tectonic regime. Intersecting faults also increased reactive surface areas of host rocks by creating a greater intensity of micro- to macro-fracturing. It is not solely fault orientation that generated ore sites, rather it is the intersection of inherently iron-rich rocks with a controlling structure, because it appears that ore deposits of all sizes plunge down the intersection of the primary layering of iron-rich host rocks with fault planes. The scale of an ore deposit therefore depended on the strike extent of that intersection: for example, faults with a generally NE orientation associated with DS4 dykes are common at Sunrise Hill, but rather than control the plunge and strike-length of iron-ore deposits there, the faults form the limits of those ore deposits. This is because strata strike generally

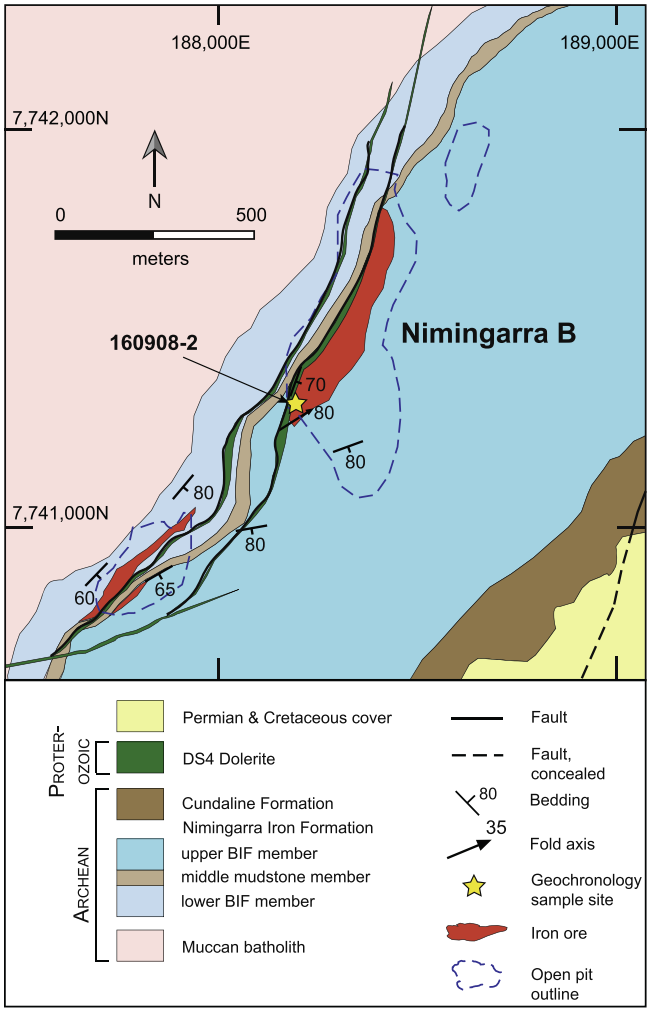

Fig. 12. Solid geology map of the Nimingarra B ore bodies. Coordinates are Map Grid of Australia 94, Zone 51.

in a SE direction such that those faults cross at a high angle to primary layering, thereby minimizing the scale of the reactive interface.

On the Nimingarra line, where primary layering in BIF varies from N-striking to NE-striking, there is a different relationship with N-trending and NE-trending faults. The structural architecture there has developed large iron-ore deposits, because the strike intersection between primary layering and fault planes is at a low angle, thereby maximizing the reactive surface. Iron-ore deposits plunge down, or rather along, the intersection and have considerable strike extent.

On the Sunrise Hill–Shay Gap line, controlling faults and primary layering in BIF strike SE. Most of the pits there have significant strike extent, because of the low-angle strike intersection between primary layering and controlling faults (Fig. 14). The only lithological control on ore genesis is that the host rocks are iron rich, regardless of whether they are from the lower or upper BIF members, or whether or not they have a close spatial relationship with units with contrasting rheology (Farrel Quartzite, the middle mudstone member, or even basement granite).

Overall, it is not strike alone that determined the size of an ore deposit; it also depended on the dip of the controlling fault relative to the dip of primary layering. Where those dips are opposite, the plunge depth of the ore deposit is finite (Fig. 14A), but if the dip contrast is small, the resulting deposit plunges to greater depth. The most favourable relationship is where the dip of the controlling fault and the dip of primary layering are close to parallel (Fig. 14B). That relationship generated ore deposits not only of long strike extent, but also of great plunge depth. Most of the iron-ore deposits of the Sunrise Hill–Shay Gap line are of that geometry, with much ore still remaining below the depth of mining. Those deposits also have moderate plunges.

Most of the documented structures in the Pilbara Craton are Archean in age, but that is not to say that Archean structures have not been reactivated; they have, particularly the array of domain-defining, NE-trending faults that developed in the same tectonic environment that produced the Lalla Rookh Basin (Fig. 1). Those structures were reactivated during deposition of the Fortescue Group and emplacement of the c. 2772 Ma Black Range Dolerite Suite.

The fault array that could feasibly be implicated in iron-ore genesis is shown in Fig. 15. The dominant trends are SE and NE, and faults associated with iron-ore deposits have the same dominant trends, although with less spread. These are the fault trends recognised during the mapping of the Nimingarra to Cundaline line, with SE-trending faults having mostly dextral oblique slip dislocation, and the two sets of generally NE-trending faults having mostly sinistral oblique-slip dislocation. Although the NE-trending set may follow Archean fundamental structures, SE-trending faults are uncommon Archean structures in the northern Pilbara Craton. The SE-trending faults offset dykes of the Black Range Dolerite Suite so they must be <c. 2772 Ma in age. The faults associated with iron-ore deposits are invariably intruded by dolerite dykes, many of which have fluidal margins or fill lows between swells on fault planes. The implication is that these dykes intruded during faulting, suggesting that the syn-ore fault arrays, whether they are new structures or reactivated structures, were generated during regional extension.

7. Description of the iron-ore

7.1. Ores in outcrop

There are two dominant ore textures in the mapped pits: laminated or brecciated iron-ore developed in BIF, what Podmore (1990) referred to as "lode type ore", and massive iron-ore developed in dolerite. In BIF, mineralisation shows a transition from barren BIF with abundant chert bands (Fig. 16A) through jaspilitic BIF with bands of grey, specular hematite replacing iron-oxide and chert bands (Fig. 16B), to low-grade ore with relict chert bands (Fig. 16C) and finally high-grade laminated iron-ore (Fig. 16D). Even where ore developed in BIF is brecciated, the ore preserves a laminated structure. In the Mount Goldsworthy pit some ore contains cavities lined by coarse-grained plates of hematite. Ore developed in dolerite is always massive. Although the proportion of laminated to massive ore can no longer be determined, there is still much massive ore adhering to bounding faults in some pits. Massive ore was developed in syn-fault DS4 dolerite dykes because these rocks were also iron rich and chemically reactive.

7.2. Petrography of the ores

Samples of the Nimingarra Iron Formation in outcrop have been strongly affected by weathering, and do not reflect the true mineralogy of the iron formation. Detailed petrography of the iron formation shows alternating layers of iron-oxides (hematite, magnetite and goethite) and silica minerals (chert and quartz). Hematite is the most abundant oxide, forming both fine-grained crystals and plates, and larger euhedral crystals after magnetite (martite). Many martite crystals contain a core or inclusions of

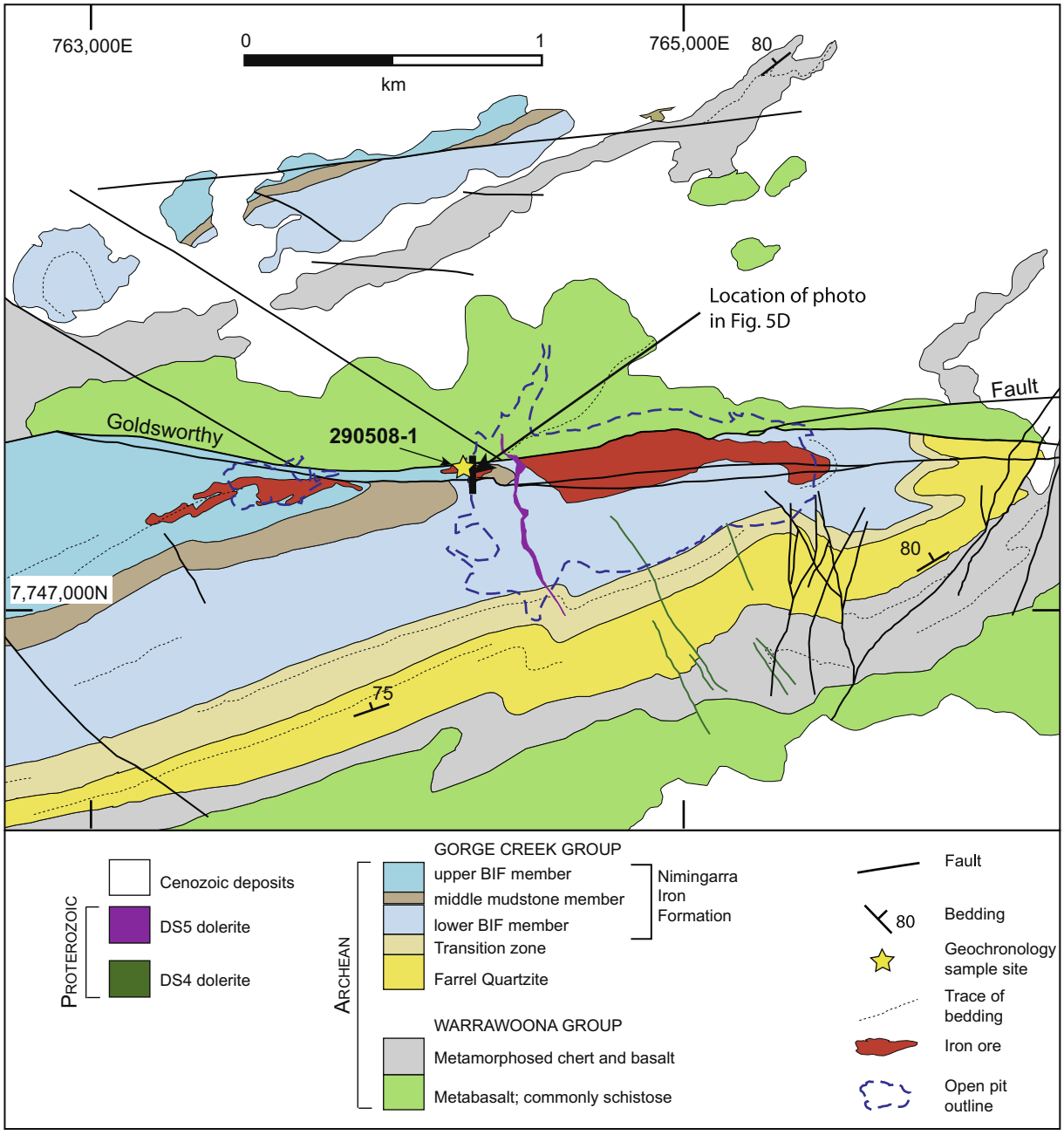

Fig. 13. Interpretive geology map of the Goldsworthy ore body. Note the location of the photo from Fig. 5D. Coordinates are Map Grid of Australia 94, Zone 50.

magnetite. The distribution of martite in most samples suggests that magnetite was the principal iron-oxide mineral in most of the iron formation before mineralisation. Much of the magnetite may have formed during regional metamorphism but the presence of veins of magnetite, coupled with the abundance of magnetite in some samples, suggests that at least some is hydrothermal in origin. Goethite is the main iron-oxide mineral in many of the most strongly weathered samples, and is also associated with late stage fractures and veins, and possibly more-modern replacement of precursor minerals such as siderite, ferroan dolomite–ankerite and iron silicates. A detailed paragenesis of the ore minerals could not be constructed because no drill core was available; all samples were taken from surface and are overprinted to varying degrees by weathering. Nevertheless, the interpreted ages of the iron minerals are discussed in relation to the regional tectonothermal events in Section 9.3.

Iron-ore from the Sunrise Hill 1, Mount Goldsworthy and Y2/3 pits was examined in detail. The ore comprises mainly hematite, which forms a dense mesh of randomly oriented plates (Fig. 17A, B). Amongst the microplaty hematite are larger blocky aggregates of hematite, possibly after magnetite. The hematite ore also contains minor quartz and chert. Hematite crystals contain abundant quartz inclusions, as well as rare inclusions of magnetite and pyrite, chalcopyrite and sphalerite. Hematite ore also contains trace amounts of xenotime, apatite and zircon. The xenotime crystals occupy interstices between the hematite plates (Fig. 17B–D), although some aggregates are embedded in densely packed hematite, indicating that some of the xenotime probably formed before the last phase of hematite growth (Fig. 17C,E). Moreover, xenotime is typically larger than surrounding pores between hematite crystals, indicating some hematite growth occurred after xenotime precipitation. Some ore samples contain cavities lined with thick

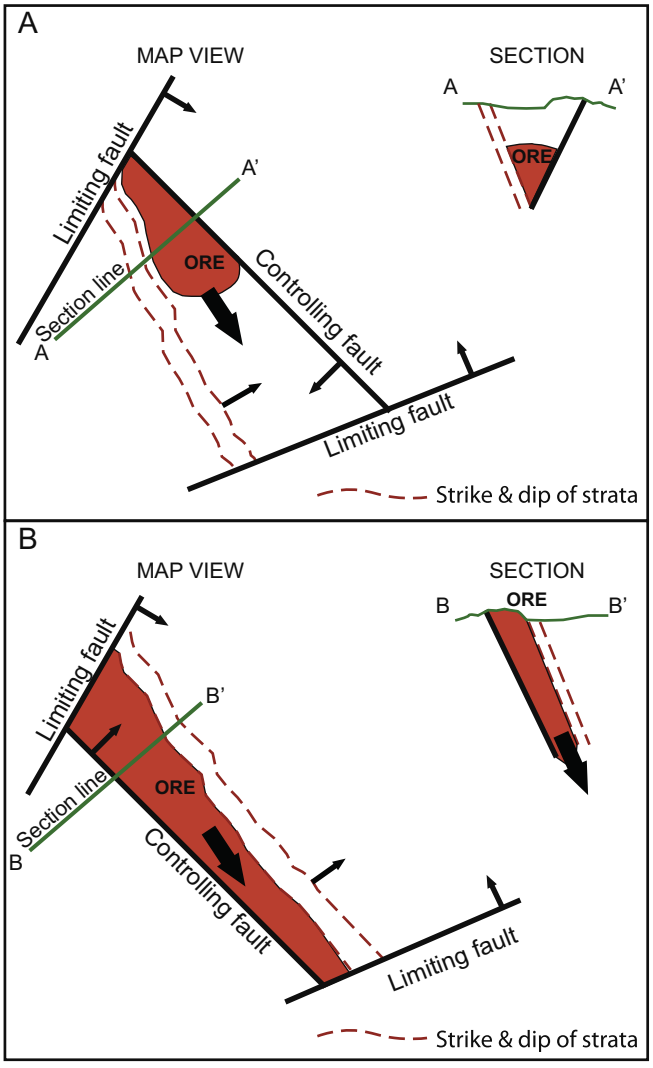

Fig. 14. Summary cartoon showing the favourable sites for iron-ore mineralisation when strata and controlling faults dip in opposite directions (A) and subparallel to each other (B).

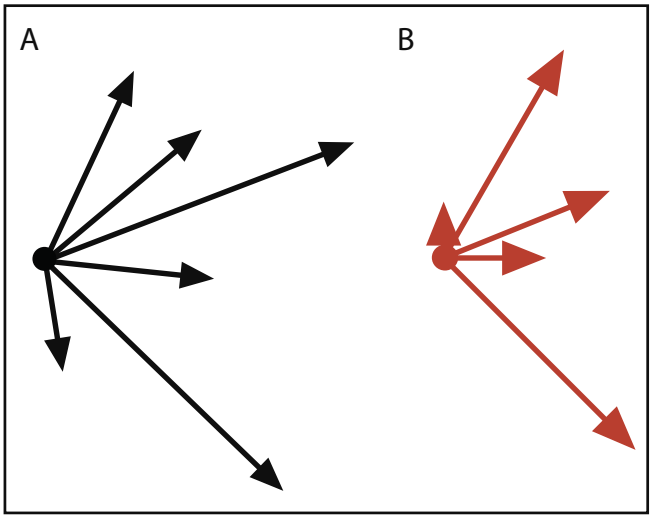

Fig. 15. Fault trends in the Nimingarra to Shay Gap line, with line length reflecting the number of faults. A) Total faults. B) Faults bounding iron-ore deposits.

rims of densely packed, coarse hematite plates and a centre composed of coarse-grained quartz crystals (Fig. 18F,G). Xenotime crystals occupy the interstices between these coarse hematite plates (Fig. 18H–K).

Samples of an iron-mineralised DS2 dolerite dyke in the Shay Gap 7 pit (Fig. 18A) were also examined. The dolerite is highly altered and comprises mainly chlorite and quartz, with minor altered skeletal ilmenite, rutile and hematite (Fig. 18B–D). Trace amounts of accessory minerals are also present, including magmatic baddeleyite, authigenic monazite, authigenic xenotime, and chalcopyrite inclusions in magmatic quartz. The matrix of the dolerite contains randomly oriented plates of secondary hematite and larger aggregates of inclusion-rich hematite. The hematite is intergrown with, and encloses, magmatic and secondary minerals in the dolerite, including chlorite, quartz, ilmenite, chalcopyrite and monazite. Anhedral, inclusion-rich monazite up to 100 μm in diameter is distributed throughout the dolerite (Fig. 18E), and is locally intergrown with hematite. Anhedral xenotime is also relatively common in the dolerite, mainly associated with altered ilmenite crystals (Fig. 18F).

8. SHRIMP U–Pb geochronology

8.1. Analytical methods, data assessment and presentation

To constrain the age of mineralisation, xenotime and monazite intergrown with hematite ore were selected for radiometric dating using SHRIMP (Table 1). Monazite and xenotime crystals large enough for analysis by SHRIMP were dated following established methodologies (Fletcher et al., 2004, 2010). Attempts were also made to date baddeleyite or zircon from the DS4 dolerite dykes, which are considered to be coeval with the iron mineralisation, but no unaltered crystals large enough to date were identified.

Polished thin sections were examined by optical microscope using transmitted, reflected and incident light. Selected polished thin sections were coated in a carbon-film and examined using a JEOL JSM-6400 scanning electron microscope (SEM) fitted with an energy dispersive X-ray spectrometer (EDS). Where xenotime and monazite suitable for dating were identified in polished thin sections, they were drilled out in ~3 mm discs and cast in 25 mm epoxy mounts for analysis by SHRIMP. Xenotime MG-1, Xeno-1 and BS-1 and monazite French, Z2908 and Z2234 were used as reference materials. The primary reference standards for calibrating Pb/U and Pb/Th ratios and U and Th concentrations for each analytical session are indicated in Table 2. The ages and compositional characteristics of the xenotime and monazite reference materials are described in detail by, respectively, Fletcher et al. (2004) and Fletcher et al. (2010). In all cases, the reference materials were in separate mounts which were cleaned and Au-coated with the sample mounts.

Data were compiled from numerous analytical sessions. Analytical parameters of all sessions are given in Table 2. All data were reduced using Squid-2 software (Ludwig, 2009). The secondary reference materials were used to correct for matrix effects following established procedures detailed by Fletcher et al. (2004, 2010). The correction for matrix effects in xenotime was based on U and Th concentrations determined by SHRIMP and an empirical factor assigned to ΣREE, as no REE data from xenotime were collected during the SHRIMP analysis. Xeno-1 and Z2908 were also used to monitor the instrumental mass fractionation in $^{207}Pb/^{206}Pb$ during analysis of xenotime and monazite, respectively.

In most cases, common Pb up to 1% (in ^{206}Pb) and discordance (determined on the basis of each $^{207}Pb/^{206}Pb$ date relative to its corresponding $^{206}Pb/^{238}U$ date, as defined in Table 3) up to 10% are tolerated. Unless specified otherwise, ages given in the follow-

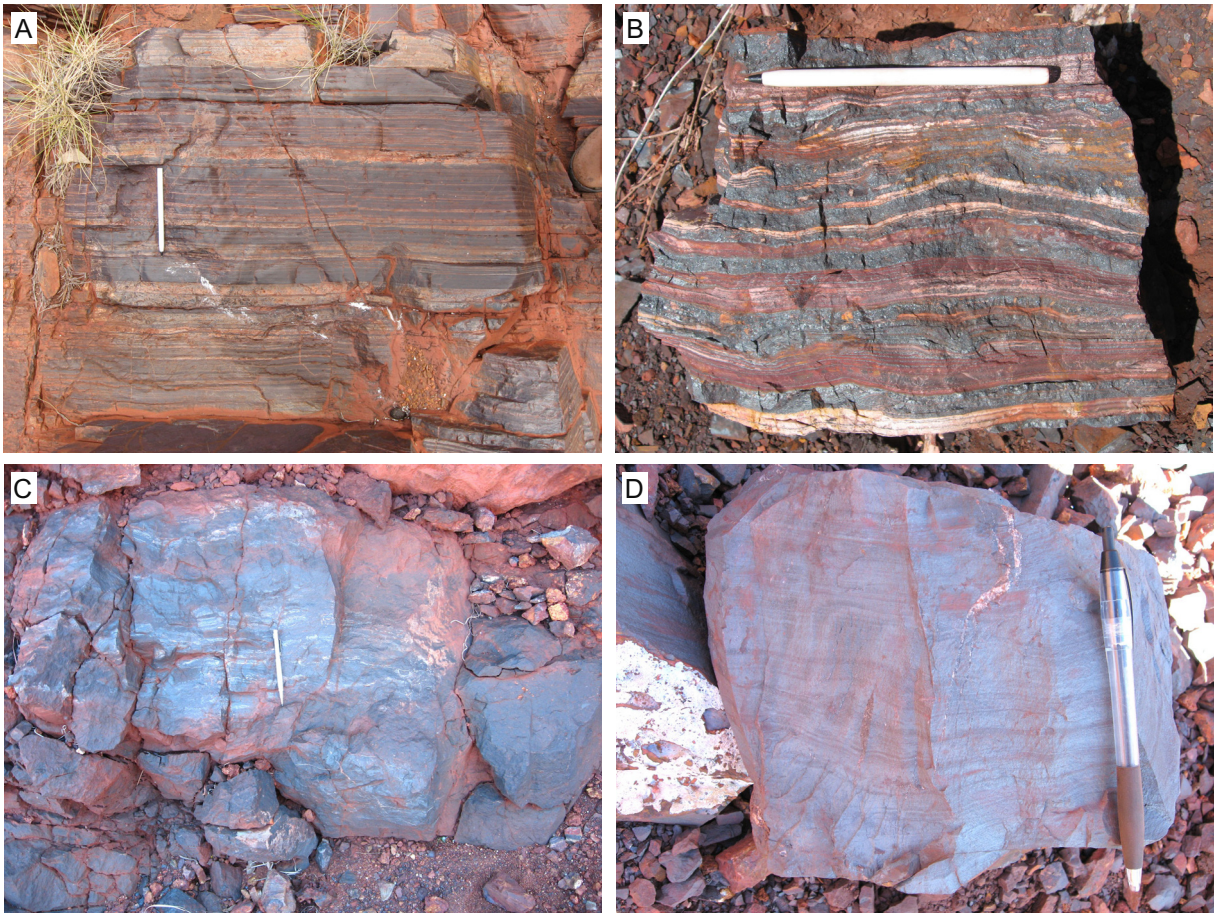

Fig. 16. A) Background (unmineralised) BIF comprising alternating layers of iron oxides and chert from Nimingarra F (at MGA94 Zone 51 187120E 7737435N. B) Proto-ore comprising iron oxide and chert layers being replaced by specular grey hematite from Nimingarra F East (at MGA94 Zone 51 187515E 7737480N). C) Remnant laminated iron-ore in the Sunrise Hill 3 pit showing preservation of silica-rich banding (at MGA94 Zone 51 193050E 7734500N). D) Laminated iron-ore from Sunrise Hill 1 (at MGA94 Zone 51 192360E 7735000N).

ing notes are weighted mean $^{207}Pb/^{206}Pb$ dates, with 95% confidence limits. Data in tables and plots are presented with 1σ precision.

8.2. Results

8.2.1. Xenotime in DS2 dolerite dyke from Shay Gap 7

Xenotime crystals or their aggregates (typically 20–50 μm across) show irregular outlines and are intergrown with secondary hematite in the dolerite dyke (Sample 291106-5; Mount 08-26) in the Shay Gap 7 pit. Fifteen analyses were carried out on six grains of xenotime in this sample. Seven analyses are concordant and have <1% common ^{206}Pb, but one of these is a young outlier (Table 3). All analyses in the main group have U <100 ppm and, therefore, yield dates with poor precision. They give a weighted mean $^{207}Pb^*/^{206}Pb^*$ date of 2243 ± 31 Ma (n = 6 [5 grains]; MSWD = 1.14) (Fig. 19A). The dated xenotime in this sample is interpreted to reflect the time of hematite mineralisation in the dyke (and by extension) in the BIF in Shay Gap 7.

8.2.2. Monazite in dolerite dyke from Nimingarra deposit B

Two grains of monazite were identified in a chlorite-altered DS4 dolerite dyke (Sample 160908-2; Mount 09-14). Five analyses of the two grains yielded overlapping U and Th concentrations with extremely low U (<20 ppm) and low Th (1080–6110 ppm) (Table 4). As a consequence, the Pb/Th dates are considered more reliable than the Pb/U or Pb/Pb dates. Grain 0914D.1 comprises two connected crystals each ~15 μm across which show subhedral to anhedral habit, whereas grain 0914E.1 grew (up to 30 μm wide) around a sulphide core, and is locally porous. The best analysis is from grain 0914D.1 which gives a $^{208}Pb^*/^{232}Th$ date of 2246 ± 48 Ma (1σ), whereas the other analysis from the same grain is disregarded given its high common Pb (f_{208} > 5%). Three analyses on grain 0914E.1 yield significantly younger $^{208}Pb^*/^{232}Th$ dates with a weighted mean of 1467 ± 40 Ma (MSWD = 0.53). However, the younger monazite grain shows anomalously (but consistently) low apparent Ce contents, so these data may be affected by an unidentified matrix problem (due to an extreme sample composition).

8.2.3. Xenotime in hematite iron ore at Yarrie mine (Y2/3 pit)

Twenty-three analyses of seven large xenotime crystals were conducted on a sample of hematite iron-ore from the Y2/3 pit (Sample 281106-8; Mount 07-29). The dated xenotime grains show irregular or subhedral habit (Fig. 17B–E) and are interstitial to hematite. Authigenic xenotime locally occurs as an overgrowth surrounding a zircon core, and is intergrown with, and enclosed by, platy hematite (Fig. 17D). Xenotime in this sample is characterised by moderate to high U (210–4550 ppm, Table 5) with Th/U varying from <0.01 to 1.05. Two analyses have high common Pb (f_{206} > 1%) and/or large discordance (disc. >10%), and hence are excluded from further discussion. Seventeen analyses are concordant or near-concordant (disc. <10%) and have <1% common ^{206}Pb (Table 5). The data are scattered (Fig. 19B), with the oldest analysis from a

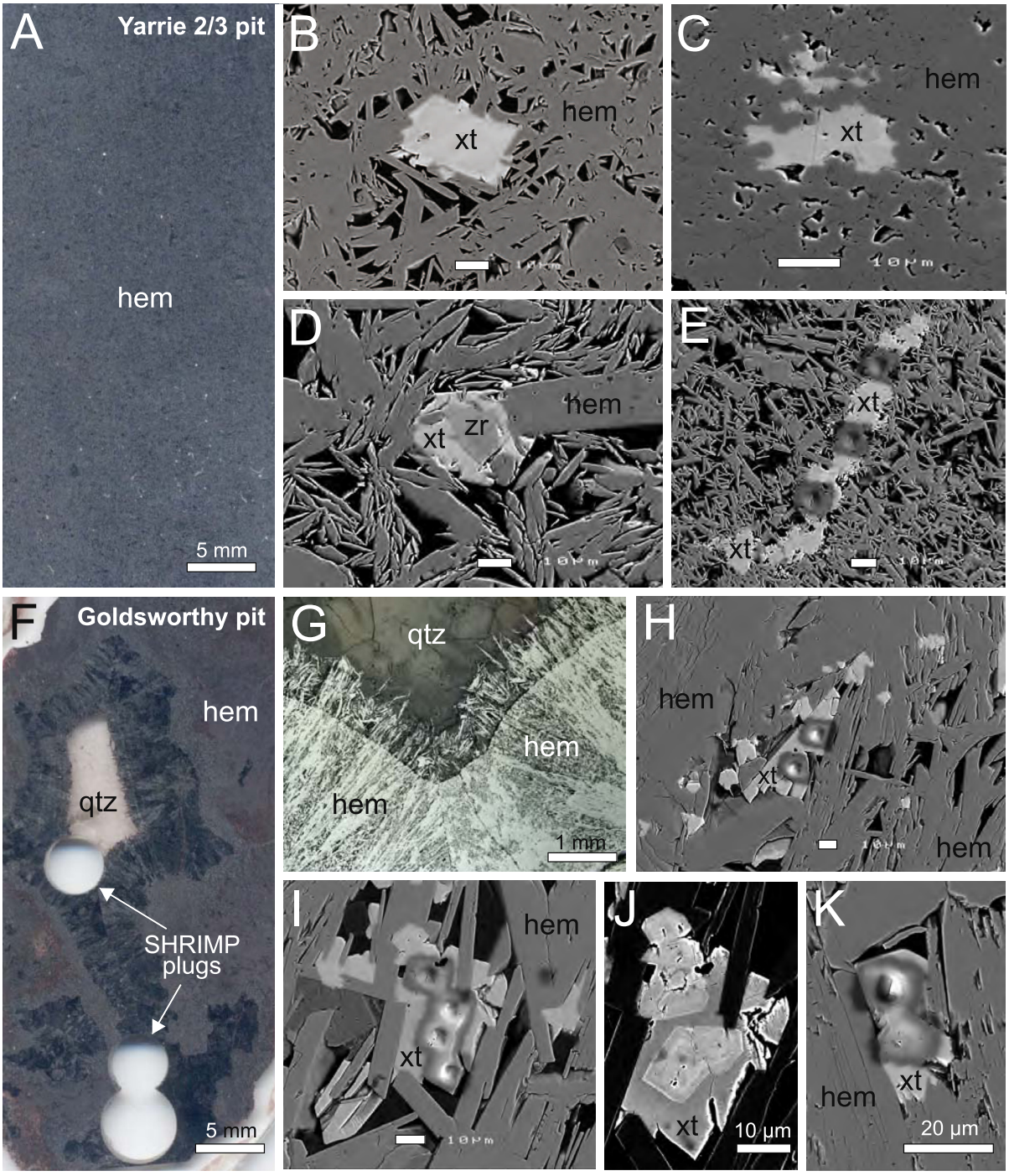

Fig. 17. A) Photograph of polished thin section of massive hematite ore from the Y2/3 pit, Yarrie. B) Back-scattered electron (BSE) image of blocky xenotime crystal (xt) in sample of hematite ore from Y2/3 pit. C) BSE image of irregular xenotime crystals (xt) enclosed in hematite (hem). D) BSE image of detrital zircon (zr) surrounded by authigenic xenotime (xt), intergrown and surrounded by platy hematite (hem). E) BSE image of elongate xenotime crystal (xt) in hematite ore comprising randomly oriented hematite plates. Note the presence of three oval SHRIMP analytical pits in xenotime. F) Photograph of polished thin section of hematite ore (hem) from Goldsworthy pit showing cavity-lining hematite and quartz (qtz). G) Reflected light image of cavity lining of hematite (hem) and blocky quartz (qtz). H) BSE image of late-stage xenotime (xt) filling cavities between hematite crystals (hem). I) BSE image of xenotime filling cavities and partly enclosed in hematite. Note presence of four oval SHRIMP analytical pits. J) BSE image of xenotime in panel I showing distinct compositional zoning comprising a brighter core and darker rim. K) BSE image of xenotime crystal (xt) within fibrous hematite crystal (hem).

single xenotime grain which yielded a $^{207}Pb^*/^{206}Pb^*$ date of 2458 ± 11 Ma (1σ). The rest have $^{207}Pb^*/^{206}Pb^*$ dates ranging from c. 2253 Ma to c. 1662 Ma, with two possible concentrations: one defined by three analyses from two grains giving a weighted mean $^{207}Pb^*/^{206}Pb^*$ date of 2249 ± 19 Ma (MSWD = 0.07); the other one defined by five analyses from four grains which yield a weighted mean $^{207}Pb^*/^{206}Pb^*$ date of 2187 ± 12 Ma (MSWD = 1.11). The remaining analyses may reflect an age mixing array towards younger age components at either c. 1800 Ma or 1600 Ma, or both.

8.2.4. Xenotime in hematite iron ore in Sunrise Hill 1 pit

Thirty-five analyses (including eight repeats) were carried out on twenty grains of xenotime in a sample of hematite ore (Sample 230608-1; Mounts 09-50 and 09-57) from the Sunrise Hill 1 pit.

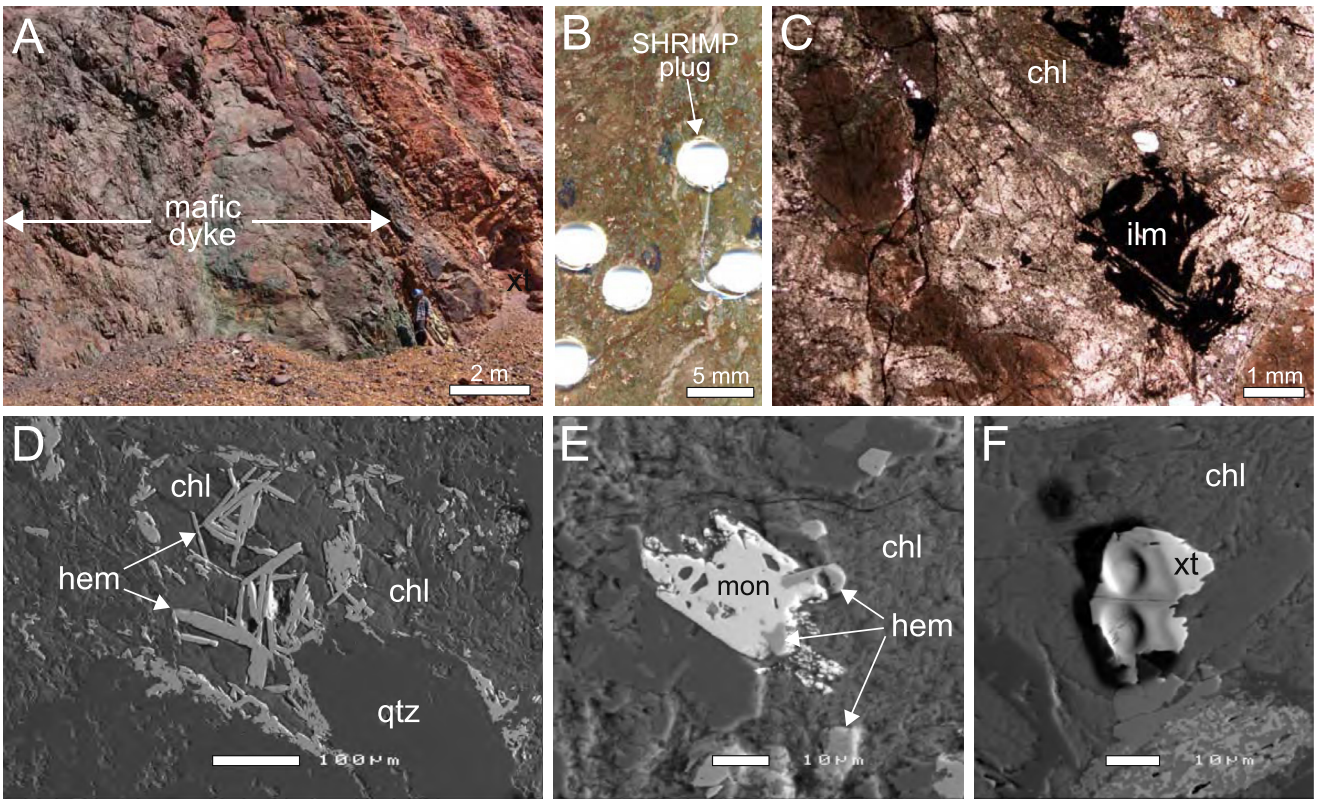

Fig. 18. A) Field photograph of an altered mafic dyke in Shay Gap 7 pit. B) Photograph of a polished thin section from the dyke featured in panel A. The section has five holes produced by removing 4-mm diameter plugs containing monazite and xenotime crystals for dating by in situ SHRIMP geochronology. C) Transmitted light image of mafic dyke showing a relict ilmenite crystal (ilm) in a matrix of chlorite (chl) and quartz. D) Back-scattered electron (BSE) image of hematite crystals (hem) in the chlorite-quartz matrix of the mafic dyke. E) BSE image of hydrothermal monazite crystal (mon) intergrown with small hematite grains (hem). F) BSE image of hydrothermal xenotime crystal (xt) with two oval SHRIMP analytical pits surrounded by rectangular raster areas.

Table 1
Summary of sample details.

Sample number	Locality	DLAT	DLONG	EASTING	NORTHING	MGA94 ZONE	Rock type	Mineral
291106-5	Shay Gap 7	−20° 28.111′	120° 04.311′	194515	7733940	51	Mineralized dolerite	xenotime
160908-2	Nimingarra B	−20° 24.081′	120° 00.747	188178	7741270	51	Mineralized dolerite	monazite
281106-8	Yarrie (Y2/3)	−20° 36.849′	120° 18.087′	218749	7718221	51	Hematite ore	xenotime
230608-1	Sunrise Hill 1	−20° 27.590′	120° 03.036′	192279	7734862	51	Hematite ore	xenotime
120908-5	Nimingarra F	−20° 26.178′	120° 00.108′	187137	7737376	51	Hematite ore	xenotime
290508-1	Goldsworthy	−20° 21.250′	119° 31.829′	764171	7747296	50	Hematite ore	xenotime

Xenotime grains in this sample are typically equant (15–30 μm in size) intergrown with and partly enclosed by hematite. The analyses suggest that there are two distinct chemical groupings amongst these data (Table 6). Six analyses on three grains have higher U (320–1170 ppm) and moderate Th (20–200 ppm); only one of these analyses is concordant, yielding a $^{207}Pb^*/^{206}Pb^*$ date of

Table 2
SHRIMP operating parameters for all analytical sessions.

Session	Date	Mount	Sample	Dated mineral	Kohler aperture (μm)	Spot (approx.) (μm)	O_2^- primary (nA)	M/ΔM (1%)	# scans	Pb/U stds	# Pb/U stds	Pb/U external precision (1σ, %)	Pb/U matrix correction (%)
1	2007/08/20	0729	281106-8	xenotime	30	10	0.2	5000	7	MG-1	12/14	2.6	−6.3
2	2008/12/17	0826	291106-5	xenotime	40	12	0.4	5000	7	MG-1	7/7	2.1	−5.9
3	2009/06/08	0914	160908-2	monazite	30	10	0.3	5200	7	French	8/10	1.4	+1.4
4	2009/11/28	0950	230608-1	xenotime	30	10	0.3	5500	7	Xeno-1	10/11	1.2	+9.8
5	2009/12/11	0957	290508-1,230608-1	xenotime	30	10	0.3	5200	7	Xeno-1	7/7	1.0	+8.5
6	2010/01/28	1003	281106-2	xenotime	30	10	0.2	5800	9	Xeno-1	32/39	2.1	+9.2

Table 3
SHRIMP U-Th-Pb data for xenotime in altered dolerite dyke in Shay Gap 7 pit (Sample 291106-5).

Analysis	U	Th	Th/U	f_{206}	Total	±1σ	Total	±1σ	$^{238}U/^{206}Pb^*$	±1σ	$^{207}Pb^*/^{206}Pb^*$	±1σ	$t[^{238}U/^{206}Pb^*]$		Disc.	$t[^{207}Pb^*/^{206}Pb^*]$	
	(ppm)	(ppm)		(%)	$^{238}U/^{206}Pb$		$^{207}Pb/^{206}Pb$						(Ma)	± 1σ	(%)	(Ma)	± 1σ
Main group																	
0826I.1-1	46	226	4.95	−0.18	2.365	0.132	0.1420	0.0027	2.495	0.147	0.1443	0.0032	2173	108	5	2280	38
0826K.1-1	49	10	0.20	0.64	2.188	0.117	0.1492	0.0026	2.326	0.132	0.1442	0.0039	2305	109	−1	2279	47
0826F.1-1	59	77	1.31	−0.18	2.405	0.128	0.1414	0.0027	2.536	0.142	0.1437	0.0031	2143	101	6	2273	38
0826G.1-2	56	1326	23.8	0.50	2.429	0.131	0.1441	0.0026	2.588	0.148	0.1403	0.0037	2106	102	6	2231	46
0826F.1-2	88	185	2.10	0.32	2.325	0.104	0.1423	0.0020	2.465	0.117	0.1402	0.0026	2195	88	2	2229	33
0826H.1-1	73	394	5.37	0.31	2.566	0.123	0.1374	0.0025	2.723	0.138	0.1354	0.0032	2017	87	7	2169	41
Young outlier																	
0826J.1-2	142	780	5.48	0.96	3.042	0.113	0.1152	0.0016	3.252	0.128	0.1074	0.0030	1728	59	2	1756	51
>10% disc.																	
0826J.1-1	327	779	2.39	0.80	4.711	0.169	0.1033	0.0022	5.035	0.192	0.0969	0.0042	1168	41	25	1565	81
f206>1%																	
0826F.1-4	102	351	3.44	1.43	2.499	0.119	0.1520	0.0023	2.682	0.135	0.1401	0.0044	2043	88	8	2228	54
0826G.1-1	41	947	23.0	1.71	2.793	0.209	0.1584	0.0085	3.009	0.240	0.1441	0.0111	1850	127	19	2277	133
0826K.1-2	138	276	2.00	2.08	2.633	0.115	0.1338	0.0019	2.844	0.133	0.1162	0.0047	1942	78	−2	1899	73
0826H.2-1	84	185	2.21	2.75	2.675	0.119	0.1470	0.0036	2.908	0.138	0.1235	0.0067	1905	78	5	2007	97
0826I.1-2	103	312	3.04	8.88	2.967	0.193	0.1685	0.0041	3.443	0.248	0.0928	0.0175	1644	104	−11	1484	356
0826F.1-3	134	402	3.00	12.73	1.933	0.111	0.2628	0.0086	2.343	0.148	0.1504	0.0179	2291	121	3	2351	204
0826K.1-3	598	564	0.94	27.29	1.676	0.208	0.4500	0.0109	2.445	0.351	0.2082	0.0498	2210	263	24	2892	388

Pb^* indicates radiogenic Pb.
f_{206} is the proportion of common Pb in ^{206}Pb, determined using the measured $^{204}Pb/^{206}Pb$ and a common Pb composition from the Stacey and Kramers (1975) model at the approximate age of the sample.
All Pb isotope data have been corrected for common Pb.
Disc. is apparent discordance, as $100(t[^{207}Pb^*/^{206}Pb^*] - t[^{238}U/^{206}Pb^*]) / t[^{207}Pb^*/^{206}Pb^*]$.
Analyses are sorted by descending $^{207}Pb^*/^{206}Pb^*$ age, except those not considered in age calculation due to high common Pb or large discordance.

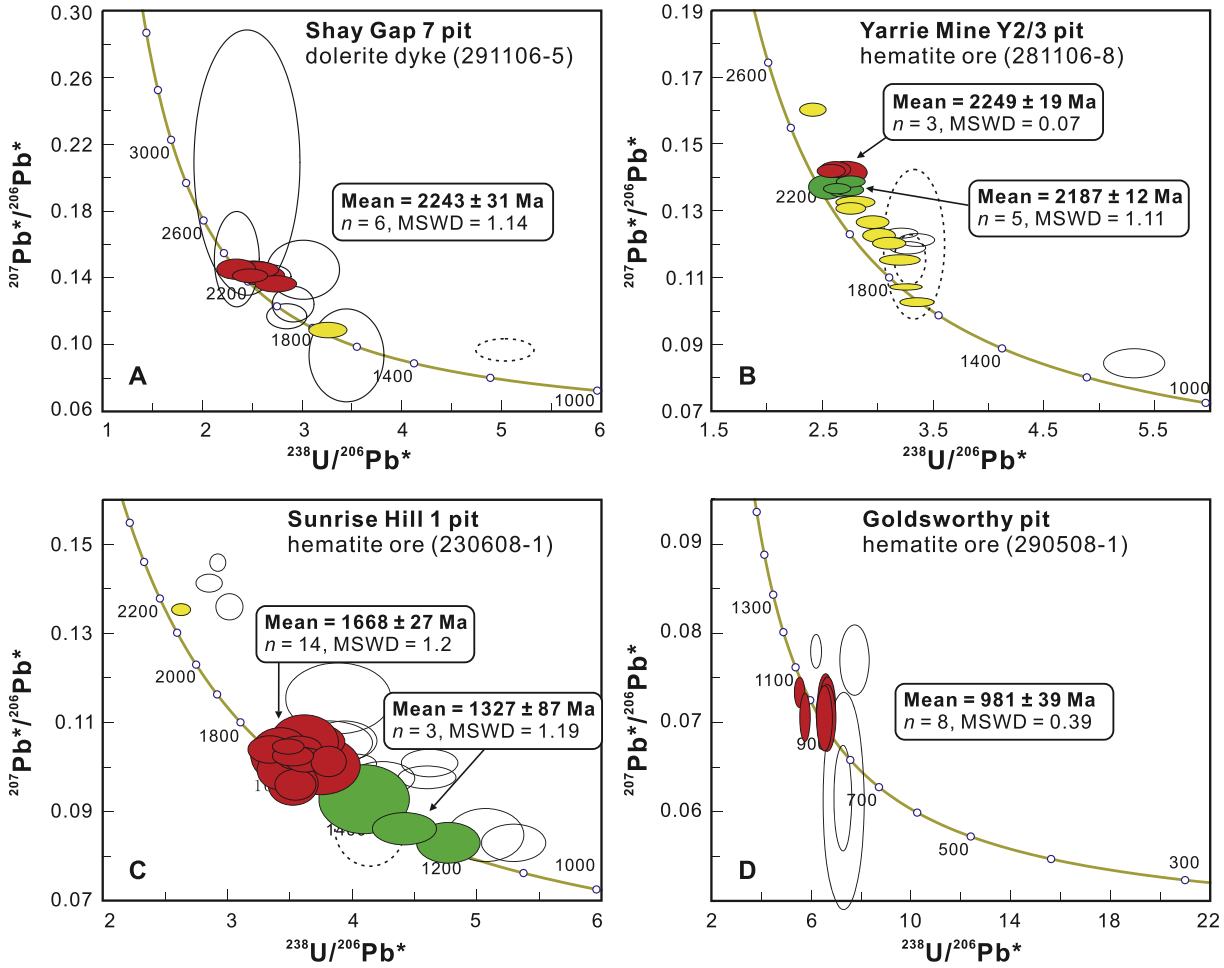

Fig. 19. Tera-Wasserburg concordia plots of SHRIMP U-Pb data for xenotime in a dolerite dyke from the Shay Gap 7 pit (A), and in hematite ore samples from the Yarrie Mine Y2/3 pit (B), Sunrise Hill 1 pit (C), and Goldsworthy pit (D). Red- and green-filled ellipses represent analyses that define an age population with weighted mean $^{207}Pb^*/^{206}Pb^*$ dates annotated next to the cluster; yellow-filled ellipses are ungrouped outliers; unfilled ellipses are analyses with >10% discordance, and dashed ellipses are those have >1% common Pb (in ^{206}Pb). Individual ellipses represent 1 σ uncertainties, whereas weighted mean dates are quoted at 95% confidence levels.

2167 ± 12 Ma (1σ), whereas the five discordant analyses returned $^{207}Pb^*/^{206}Pb^*$ dates ≥ 2170 Ma. The other grains have consistently low U (<300 ppm) and Th (<10 ppm); analyses from these grains yielded $^{207}Pb^*/^{206}Pb^*$ dates ranging from c. 1720 Ma to c. 1255 Ma, with a main population at 1668 ± 27 Ma (n = 14, MSWD = 1.2) (Fig. 19C). The sample also contains a xenotime core dated at c. 2160 Ma, implying that hematite growth in this deposit commenced at about that time.

8.2.5. Xenotime in hematite iron-ore from Nimingarra deposit F

Five analyses were carried out on five grains of xenotime in this sample of iron ore (Sample 120908-5; Mount 10-03). Three of the dated xenotime grains (1003A.1, B.1, and J.1) are euhedral, 20–30 μm long, and with aspect ratios of 2:1. The other two grains (1003 K.1 and K.2) show irregular outlines but are of similar size to the euhedral grains. Irrespective of the habit, these xenotime grains can be divided into two groups: two grains have relatively high U (266 and 315 ppm) and Th (26 and 36 ppm), the other three grains yield lower U (<200 ppm) and extremely low Th (<1 ppm). Data from the two grains with relatively high Th are discordant. The three Th-depleted grains yielded concordant data (within 1σ) and have <1.05% common ^{206}Pb (Table 7). Their $^{207}Pb/^{206}Pb$ data are rather imprecise but indicate a crystallisation age of c. 1000 Ma. The $^{206}Pb^*/^{238}U$ data from the three grains yield a weighted mean date of 1042 ± 46 Ma (2σ, MSWD = 2.8).

8.2.6. Xenotime in hematite iron-ore, Goldsworthy pit

Xenotime in this sample is up to 50 μm across, and is restricted to the coarse-grained platy hematite that lines cavities (Fig. 17F–K). The xenotime crystals comprise a brighter euhedral core (in back-scattered electron images) enclosed by a darker, anhedral rim (Fig. 17J). The rim partly encloses adjacent hematite plates. Twelve analyses were obtained from six xenotime crystals from a sample of hematite ore in the Goldsworthy pit (Sample 290508-1; Mount 09-57). All except one of the analysed grains are characterised by low Th concentrations (<1 ppm), similar to c. 1000 Ma xenotime from the Nimingarra Deposit F (Table 8). Three analyses are discordant, and one analysis with the lowest U concentration shows poor precision. These are disregarded for the age determination. The remaining eight analyses from five grains are <10% discordant (except 0957F.1–3 which is -11% discordant but within 1σ from the concordia), have <1% common ^{206}Pb (Table 8) and yield a weighted mean $^{207}Pb^*/^{206}Pb^*$ date of 981 ± 39 Ma (MSWD = 0.39) (Fig. 19D).

9. Discussion

9.1. Timing of hematite mineralisation

Any geochronological study of iron ores in the northern Pilbara Craton will be hampered by a combination of the scarcity of xeno-

Table 4
SHRIMP U-Th-Pb data for monazite in dolerite in Nimingarra Deposit B (Sample 160908-2).

Analysis	U	Th	Th/U	f_{206}	f_{208}	$^{207}Pb/^{206}Pb$	±1σ	$^{206}Pb/^{238}U$	±1σ	$^{208}Pb/^{232}Th$	±1σ	$^{207}Pb^*/^{206}Pb^*$	±1σ	$^{206}Pb^*/^{238}U$	±1σ	$^{208}Pb^*/^{232}Th$	±1σ	t $[^{207}Pb^*/^{206}Pb^*]$	±1σ	t $[^{206}Pb^*/^{238}U]$	±1σ	t $[^{208}Pb^*/^{232}Th]$	±1σ
	(ppm)	(ppm)		(%)	(%)	Total		Total		Total								(Ma)		(Ma)		(Ma)	
0914D.1-1	5	1080	205	56.42	5.85	0.5956	0.0157	1.1849	0.1148	0.1310	0.0023	0.0402	0.1443	0.5214	0.0858	0.1248	0.0030			2705	354	2377	54
0914D.1-2	15	2053	137	8.19	0.46	0.1437	0.0063	0.4394	0.0283	0.1168	0.0019	0.0750	0.0277	0.4074	0.0277	0.1175	0.0026	1068	743	2203	126	2246	48
Low $CePO_2^+$ count rate																							
0914E.1-1	19	6107	323	1.64	0.04	0.1578	0.0124	0.3018	0.0297	0.0769	0.0012	0.1433	0.0333	0.2937	0.0308	0.0766	0.0017	2267	401	1660	152	1493	33
0914E.1-2	4	1562	367	17.65	1.05	0.4439	0.0771	0.6507	0.1525	0.0751	0.0018	0.2933	0.1342	0.5338	0.1225	0.0746	0.0021			2758	495	1454	39
0914E.1-3	7	3383	496	18.30	0.35	0.1582	0.0216	0.3683	0.0738	0.0745	0.0015	0.0064	0.1570	0.2973	0.0794	0.0742	0.0019			1678	383	1447	35

f_{208} is the proportion of common Pb in ^{208}Pb, determined using the measured $^{204}Pb/^{206}Pb$ and $^{206}Pb/^{208}Pb$, and a common Pb composition from the Stacey and Kramers (1975) model at the approximate age of the sample.
Other footnotes as in Table 3.

time within the ores, the small size of most of the crystals, and the low U and high common Pb contents of many crystals. Despite these difficulties, enough data were obtained to provide reliable dates (or indicative dates) for hematite mineralisation in the Shay Gap and Goldsworthy belts (Fig. 20). The significance of the results is that, although all supracrustal host rocks are Archean in age and the principal deformations were also Archean in age, all mineralisation ages are Proterozoic.

Xenotime intergrown with microplaty hematite ore in the Shay Gap 7 deposit is dated at 2243 ± 31 Ma. This date is interpreted as the time of crystallisation of the xenotime and, by extension, of the hematite ore. Xenotime in the Yarrie (Y2/3) hematite iron-ore deposit yields a complex pattern of ages with two clusters at 2249 ± 19 Ma and 2187 ± 12 Ma, indicating two episodes of xenotime and concomitant hematite growth. A single analysis on xenotime in hematite iron ore from the Sunrise Hill 1 pit returned an age of 2167 ± 12 Ma (1σ). These results indicate initial phases of hematite growth at about 2250 Ma and 2180 Ma.

Xenotime intergrown with hematite in a sample of iron ore from the Sunrise Hill 1 pit yielded a major peak at 1667 ± 17 Ma, which indicates a likely hematite growth or remobilisation event of that age. Xenotime analyses from the Y2/3 hematite ore sample also record scattered ages between c. 2130 Ma and c. 1660 Ma, possibly reflecting this later remobilisation.

Xenotime intergrown with hematite iron ore from the Goldsworthy pit gives a unimodal age population with a weighted mean at 981 ± 39 Ma. The dated xenotime was drilled out from cavities in microplaty hematite ore that were lined with coarse-grained hematite. The xenotime date probably records this episode of iron recrystallisation/upgrading. In addition, xenotime from the Nimingarra F deposit indicates a crystallisation age of c. 1000 Ma, lending support to the interpretation of ore formation or upgrading at about that time.

Overall, in situ SHRIMP U–Pb dating indicates that xenotime grew during multiple discrete events (Fig. 20). Ore genesis commenced as early as c. 2250 Ma during regional extension, with subsequent hydrothermal remobilisation and/or mineralisation at c. 2180 Ma, c. 1670 Ma and c. 1000 Ma. The hematite ore bodies formed at sites of repeatedly focused hydrothermal fluid flow and, therefore, it is likely that iron-ore formation was probably a multi-stage process. The geochronology is consistent with the results of the mapping, which shows that hematite mineralisation in the deposits is strongly controlled by structure, and in many cases by dolerite dykes. Although only a few deposits have been dated, iron-ore in undated deposits shares the same field relationships as those where ores have been dated, implying that mineralisation occurred at similar times across the deposits.

Earlier work on the iron-ore deposits of the northern Pilbara Craton suggested that iron mineralisation was related to supergene (weathering) processes (Podmore, 1990; Waters, 1998). Goethite was interpreted to be an early formed mineral that was subsequently converted to hematite or platy hematite during burial metamorphism, with further modification of the iron-ore following subsequent exhumation and exposure. Both authors applied the supergene model of Morris (1985) from Hamersley ores to the ores in the Pilbara Craton. The radiometric ages presented here imply that hematite ore formation was not the result of supergene processes, but rather the product of multiple, Proterozoic hydrothermal events (Fig. 20).

Recently, Duuring et al. (2016) presented the results of a study on several goethite–martite-rich ore bodies across the Pilbara Craton. They suggested that all deposits shared the following evolution: (1) an initial stage of magnetite formation related to faults and shear zones at c. 2955–2920 Ma during the North Pilbara Orogeny; (2) formation of microplaty hematite and martite from hot, oxidised fluids during the Paleoproterozoic (speculated to be at

Table 5
SHRIMP U-Th-Pb data for xenotime in hematite ore from the Y2/3 pit (Sample 281106-8).

Analysis	U	Th	Th/U	f_{206}	Total	±1σ	Total	±1σ	$^{238}U/^{206}Pb^*$	±1σ	$^{207}Pb^*/^{206}Pb^*$	±1σ	t[$^{238}U/^{206}Pb^*$]		Disc.	t [$^{207}Pb^*/^{206}Pb^*$]	
	(ppm)	(ppm)		(%)	$^{238}U/^{206}Pb$		$^{207}Pb/^{206}Pb$						(Ma)	±1σ	(%)	(Ma)	±1σ
0729D.1-1	881	30	0.03	0.00	2.261	0.070	0.1610	0.0010	2.399	0.079	0.1602	0.0011	2246	62	9	2458	11
0729C.1-2	507	7.4	0.01	0.10	2.455	0.082	0.1437	0.0013	2.604	0.093	0.1421	0.0014	2095	63	7	2253	17
0729I.1-7	685	63	0.09	0.07	2.419	0.076	0.1430	0.0011	2.567	0.085	0.1417	0.0011	2121	60	6	2248	14
0729I.1-1	522	74	0.14	0.07	2.547	0.114	0.1425	0.0020	2.701	0.128	0.1412	0.0021	2030	82	9	2242	25
0729A.2-1	1287	578	0.45	0.12	2.575	0.076	0.1402	0.0008	2.744	0.086	0.1385	0.0009	2003	54	9	2208	12
0729C.1-1	215	15	0.07	−0.09	2.393	0.100	0.1367	0.0021	2.530	0.112	0.1368	0.0022	2147	80	2	2188	28
0729I.1-4	1171	163	0.14	0.04	2.464	0.072	0.1374	0.0008	2.620	0.081	0.1363	0.0009	2084	55	4	2181	11
0729A.1-2	1196	390	0.33	0.10	2.564	0.076	0.1376	0.0009	2.730	0.086	0.1360	0.0010	2012	54	8	2177	13
0729I.1-10	1148	68	0.06	0.01	2.513	0.074	0.1367	0.0012	2.671	0.083	0.1359	0.0013	2050	55	6	2176	16
0729I.1-5	898	203	0.23	0.00	2.625	0.104	0.1329	0.0010	2.787	0.117	0.1322	0.0010	1976	71	7	2128	13
0729I.1-14	803	93	0.12	−0.04	2.589	0.079	0.1307	0.0009	2.746	0.089	0.1304	0.0010	2002	56	5	2104	13
0729I.1-2	674	93	0.14	0.03	2.773	0.087	0.1271	0.0011	2.941	0.098	0.1263	0.0011	1887	54	8	2047	16
0729I.1-3	805	143	0.18	0.22	2.820	0.087	0.1248	0.0010	2.999	0.099	0.1222	0.0012	1855	53	7	1988	18
0729I.1-6	815	329	0.40	0.03	2.911	0.089	0.1207	0.0010	3.091	0.100	0.1199	0.0010	1807	51	8	1955	15
0729A.1-1	1678	551	0.33	0.15	2.986	0.107	0.1167	0.0007	3.189	0.121	0.1149	0.0009	1758	58	6	1878	13
0729B.1-3	4542	20	0.00	0.02	3.008	0.083	0.1073	0.0004	3.245	0.096	0.1067	0.0005	1732	45	1	1743	8
0729B.1-2	1809	171	0.09	0.07	3.136	0.090	0.1032	0.0007	3.346	0.103	0.1021	0.0007	1686	45	−1	1662	14
Disc. >10%																	
0729H.1-1	695	280	0.40	0.00	3.074	0.095	0.1190	0.0011	3.261	0.107	0.1184	0.0011	1724	49	11	1933	16
0729I.1-8	1540	491	0.32	0.03	3.005	0.087	0.1238	0.0008	3.203	0.099	0.1230	0.0008	1751	47	12	2000	12
0729B.1-1	635	123	0.19	0.30	4.999	0.162	0.0865	0.0024	5.317	0.183	0.0836	0.0027	1111	35	13	1283	63
0729I.1-9	1039	1082	1.04	0.17	3.136	0.094	0.1229	0.0010	3.344	0.107	0.1208	0.0011	1687	47	14	1969	17
f206 >1%																	
0729I.1-11	1058	244	0.23	1.13	3.063	0.081	0.1259	0.0025	3.292	0.093	0.1154	0.0045	1710	42	9	1886	71
0729I.1-12	1307	1078	0.83	1.76	3.065	0.154	0.1361	0.0113	3.325	0.181	0.1201	0.0139	1695	81	13	1957	207

Footnotes as in Table 3.

Table 6
SHRIMP U-Th-Pb data for xenotime in altered dolerite dyke in Sunrise Hill 1 pit (Sample 230608-1).

Analysis	U	Th	Th/U	f_{206}	Total	±1σ	Total	±1σ	$^{238}U/^{206}Pb^*$	±1σ	$^{207}Pb^*/^{206}Pb^*$	±1σ	t[$^{238}U/^{206}Pb^*$]		Disc.	t [$^{207}Pb^*/^{206}Pb^*$]	
	(ppm)	(ppm)		(%)	$^{238}U/^{206}Pb$		$^{207}Pb/^{206}Pb$						(Ma)	±1σ	(%)	(Ma)	±1σ
Old outlier																	
0950C.1-1	631	46	0.07	0.09	2.870	0.061	0.1357	0.0009	2.613	0.050	0.1352	0.0010	2089	34	4	2167	12
Main group (in 207Pb/206Pb sequence)																	
0950B.5-1	68	1	0.02	0.00	3.987	0.256	0.1050	0.0033	3.615	0.211	0.1053	0.0033	1575	81	8	1720	58
0950G.1-1b	69	1	0.01	0.00	3.979	0.220	0.1050	0.0045	3.607	0.181	0.1053	0.0045	1577	70	8	1719	79
0957D.1-1	283	6	0.02	0.00	3.803	0.102	0.1039	0.0012	3.479	0.085	0.1043	0.0012	1629	35	4	1702	22
0950K.1-1	158	2	0.02	0.17	3.928	0.143	0.1052	0.0016	3.568	0.118	0.1040	0.0020	1593	46	6	1696	35
0950K.2-1b	157	3	0.02	0.22	3.664	0.142	0.1052	0.0018	3.330	0.117	0.1036	0.0023	1693	52	0	1690	41
0950G.1-1	85	1	0.01	0.83	3.738	0.192	0.1094	0.0026	3.417	0.160	0.1024	0.0045	1655	68	1	1669	81
0950J.1-1	139	0	0.00	0.42	3.914	0.152	0.1057	0.0018	3.564	0.126	0.1023	0.0026	1594	50	4	1667	46
0957C.1-1x	169	3	0.02	−0.08	3.851	0.130	0.1011	0.0015	3.517	0.109	0.1021	0.0017	1613	44	3	1663	30
0950A.1-1	264	1	0.00	0.24	3.973	0.130	0.1030	0.0016	3.614	0.107	0.1012	0.0020	1575	41	4	1646	37
0957C.1-2	262	4	0.02	0.23	4.149	0.112	0.1025	0.0023	3.804	0.094	0.1008	0.0025	1505	33	8	1640	46
0950D.1-1	62	1	0.02	0.76	4.101	0.248	0.1061	0.0028	3.746	0.206	0.0998	0.0047	1525	74	6	1621	88
0957C.1-1	102	3	0.03	0.67	3.725	0.158	0.1044	0.0020	3.427	0.133	0.0989	0.0033	1651	56	−3	1604	63
0950B.2-1	139	1	0.01	0.83	3.844	0.161	0.1028	0.0020	3.516	0.134	0.0958	0.0036	1614	54	−4	1544	71
0950K.2-1	197	3	0.02	0.61	3.874	0.133	0.1006	0.0016	3.536	0.110	0.0956	0.0026	1605	44	−4	1540	50
Young cluster																	
0950B.1-1	65	3	0.04	0.96	4.469	0.289	0.1003	0.0030	4.091	0.241	0.0923	0.0057	1410	74	4	1473	118
0950B.6-1b	134	5	0.03	0.30	4.856	0.206	0.0880	0.0019	4.417	0.170	0.0856	0.0027	1316	46	1	1330	61
0950B.6-1	177	8	0.05	0.81	5.216	0.205	0.0890	0.0018	4.770	0.170	0.0824	0.0033	1227	40	2	1255	79
Disc. ≥10%																	
0957D.1-2x	223	2.3	0.01	0.06	3.949	0.102	0.1068	0.0013	3.614	0.086	0.1067	0.0014	1575	33	10	1743	24
0957D.1-2	233	6.2	0.03	−0.06	3.994	0.117	0.1056	0.0014	3.651	0.098	0.1064	0.0015	1561	37	10	1739	25
0950L.1-1	104	2.9	0.03	0.73	5.551	0.245	0.0902	0.0025	5.070	0.204	0.0842	0.0044	1160	43	11	1297	101
0950B.4-1b	194	5.7	0.03	0.57	5.806	0.206	0.0870	0.0019	5.297	0.171	0.0824	0.0031	1115	33	11	1255	73
0957G.1-1	235	7.1	0.03	0.12	4.397	0.129	0.1011	0.0014	4.026	0.108	0.1004	0.0016	1430	34	12	1631	30
0950B.5-1b	58	1.2	0.02	0.00	4.203	0.280	0.1048	0.0036	3.810	0.230	0.1051	0.0036	1503	80	12	1715	63
0950H.1-1	328	23	0.07	0.17	3.121	0.085	0.1424	0.0013	2.839	0.070	0.1413	0.0015	1946	41	13	2243	18
0950B.4-1	125	3.0	0.02	0.18	4.666	0.209	0.0983	0.0022	4.238	0.172	0.0971	0.0027	1366	50	13	1569	53
0957H.1-2	1168	193	0.17	0.01	2.596	0.039	0.1766	0.0018	2.390	0.033	0.1771	0.0018	2253	26	14	2626	17
0957H.1-1	992	155	0.16	0.02	2.663	0.079	0.1727	0.0023	2.449	0.066	0.1731	0.0023	2208	51	15	2588	22
0950H.1-1b	344	26	0.07	0.08	3.307	0.088	0.1363	0.0021	3.005	0.073	0.1359	0.0022	1852	39	15	2176	28
0950K.1-2	92	2.5	0.03	−0.49	4.358	0.213	0.1011	0.0022	3.932	0.174	0.1055	0.0033	1461	58	15	1724	57
0957H.1-3	955	144	0.15	0.02	3.166	0.050	0.1456	0.0014	2.910	0.042	0.1459	0.0014	1904	24	17	2298	17
0950J.2-1	160	5.6	0.04	0.00	5.070	0.186	0.0970	0.0019	4.598	0.153	0.0973	0.0019	1269	38	19	1572	36
0950J.1-2	44	0.5	0.01	0.46	4.265	0.339	0.1189	0.0043	3.883	0.281	0.1151	0.0059	1477	95	22	1882	92
0957C.1-2x	225	4.9	0.02	0.21	5.041	0.180	0.1020	0.0018	4.619	0.151	0.1005	0.0022	1263	37	23	1634	41
f206 >1%																	
0950B.3-1	105	11	0.10	2.01	4.478	0.223	0.1031	0.0025	4.143	0.189	0.0862	0.0064	1394	57	−4	1342	143

Footnotes as in Table 3.

Table 7
SHRIMP U-Th-Pb data for xenotime in hematite ore from the Nimingarra Deposit F (Sample 120908-1).

Analysis	U	Th	Th/U	f_{206}	Total	±1σ	Total	±1σ	$^{238}U/^{206}Pb^*$	±1σ	$^{207}Pb^*/^{206}Pb^*$	±1σ	t[$^{238}U/^{206}Pb^*$]		Disc.	t [$^{207}Pb^*/^{206}Pb^*$]	
	(ppm)	(ppm)		(%)	$^{238}U/^{206}Pb$		$^{207}Pb/^{206}Pb$						(Ma)	±1σ	(%)	(Ma)	±1σ
High Th																	
1003A.1-1	315	26	0.08	0.12	3.849	0.218	0.1156	0.0042	3.509	0.181	0.1146	0.0043	1617	73	14	1874	67
1003B.1-1	266	36	0.13	0.18	4.377	0.153	0.1066	0.0027	3.991	0.127	0.1051	0.0030	1441	41	16	1716	52
Low Th																	
1003J.1-1	107	0.09	0.00	−0.87	5.913	0.319	0.0717	0.0021	5.327	0.263	0.0791	0.0047	1109	50	6	1175	118
1003K.2-1	197	0.76	0.00	0.54	6.046	0.250	0.0760	0.0017	5.529	0.209	0.0716	0.0031	1072	37	−10	975	88
1003K.1-1	196	0.46	0.00	1.05	6.642	0.294	0.0757	0.0018	6.105	0.247	0.0670	0.0043	978	37	−17	839	135

Footnotes as in Table 3.

Table 8
SHRIMP U-Th-Pb data for xenotime in hematite ore from the Goldsworthy pit (Sample 290508-1).

Analysis	U	Th	Th/U	f_{206}	Total	±1σ	Total	±1σ	$^{238}U/^{206}Pb^*$	±1σ	$^{207}Pb^*/^{206}Pb^*$	±1σ	t[$^{238}U/^{206}Pb^*$]		Disc.	t [$^{207}Pb^*/^{206}Pb^*$]	
	(ppm)	(ppm)		(%)	$^{238}U/^{206}Pb$		$^{207}Pb/^{206}Pb$						(Ma)	±1σ	(%)	(Ma)	±1σ
Main group																	
0957F.1-2	271	0.08	0.0003	0.00	5.959	0.167	0.0730	0.0012	5.451	0.140	0.0733	0.0012	1086	26	−6	1021	34
0957F.1-1	158	0.04	0.0003	0.19	7.097	0.254	0.0733	0.0019	6.499	0.213	0.0720	0.0025	923	28	6	986	70
0957F.3-1	223	0.04	0.0002	0.26	7.196	0.219	0.0738	0.0016	6.597	0.184	0.0719	0.0022	910	24	7	983	62
0957E.1-1	165	0.34	0.0021	0.18	7.190	0.251	0.0730	0.0018	6.584	0.210	0.0717	0.0024	912	27	7	979	67
0957F.2-1	233	0.00	0.0000	0.12	6.980	0.206	0.0717	0.0015	6.390	0.173	0.0709	0.0018	937	24	2	955	51
0957F.1-3	283	2.82	0.0099	0.36	6.180	0.170	0.0732	0.0013	5.674	0.143	0.0704	0.0020	1046	24	−11	941	58
0957B.1-1	123	0.14	0.0012	0.22	7.165	0.285	0.0720	0.0020	6.562	0.239	0.0704	0.0027	914	31	3	939	80
0957F.2-2	152	0.01	0.0001	0.33	7.046	0.252	0.0729	0.0018	6.462	0.212	0.0703	0.0027	928	28	1	938	78
Disc. >10%																	
0957B.1-1x	130	0.11	0.0008	0.93	7.820	0.276	0.0687	0.0020	7.213	0.235	0.0613	0.0043	837	26	−29	649	152
0957F.4-1	63	0.01	0.0002	0.00	8.409	0.473	0.0766	0.0029	7.681	0.395	0.0769	0.0029	789	38	29	1118	76
0957F.1-4	316	0.22	0.0007	−0.08	6.691	0.173	0.0770	0.0012	6.117	0.145	0.0779	0.0014	976	21	15	1143	35
Low U, poor precision																	
0957F.3-2	28	0.01	0.0005	0.96	7.844	0.651	0.0686	0.0040	7.233	0.552	0.0610	0.0089	835	59	−31	638	315

Footnotes as in Table 3.

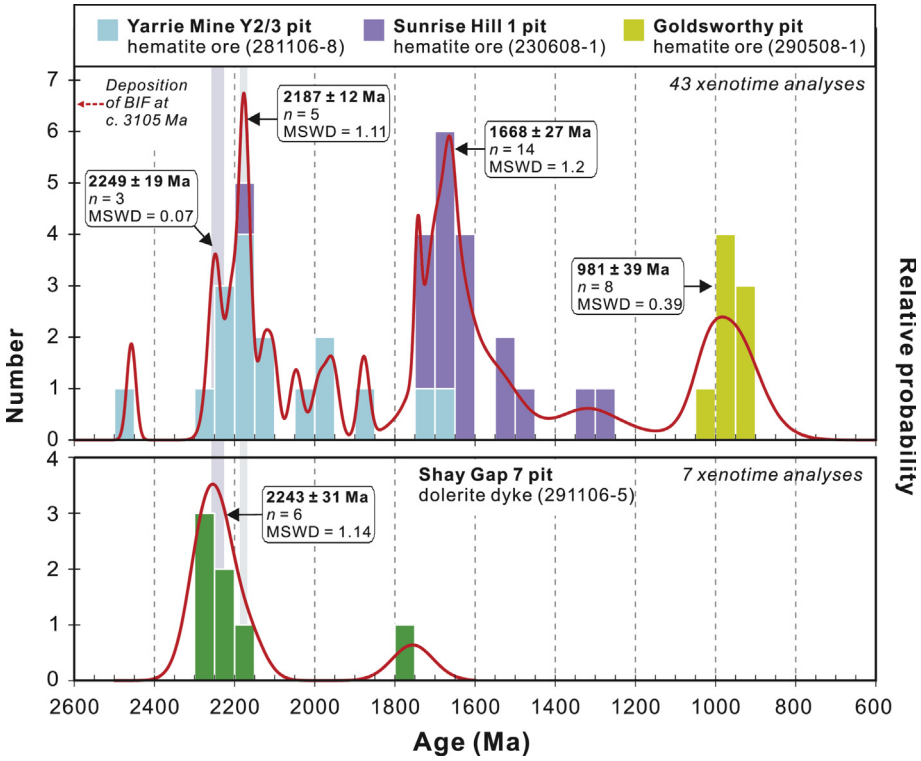

Fig. 20. Normalised probability plots and histograms (bin width = 50 Ma) for hydrothermal xenotime in hematite ore from three localities, the Yarrie Mine (Y2/3), Sunrise Hill 1, and Goldsworthy (upper panel) and a dolerite dyke from the Shay Gap 7 pit (lower panel) in the Shay Gap and Goldsworthy belts. Annotated ages are weighted mean $^{207}Pb^{*}/^{206}Pb^{*}$ dates quoted at 95% confidence levels. Only analyses with ≤1% common Pb (in ^{206}Pb) and <10% discordance are plotted.

2215–2145 Ma); (3) martite and goethite formed during tropical weathering at c. 70–50 Ma; and (4) massive to botryoidal goethite related to semi-arid weathering. Teitler et al. (2017) have also suggested that initial sub-economic enrichment of BIF in the Wodgina deposit was related to the North Pilbara Orogeny. However, in the absence of radiometric ages, the proposed relationships between hydrothermal events and given tectonothermal events are necessarily speculative. Our work indicates that the period 2250–2180 Ma was an important time for hematite ore formation in the Pilbara Craton, but that there was also an extended history of episodic Proterozoic hydrothermal events (Fig. 20) before any Cenozoic supergene overprint.

9.2. Comparison with hematite ores of the Hamersley Group

Xenotime from the Mount Tom Price high-grade, hematite iron-ore deposit in the Hamersley Province records up to eight populations, with the oldest at 2145 ± 28 Ma (Rasmussen et al., 2007a). Two other well-defined populations at 2052 ± 13 Ma and 845 ± 20 Ma are present in the xenotime data (along with a possible event at c. 1840 Ma), and a further three were identified at 1673 ± 15 Ma, 1589 ± 11 Ma and 1538 ± 12 Ma using an unmixing algorithm (Rasmussen et al., 2007a). The age spectrum at Mount Tom Price is considered by Rasmussen et al. (2007a) to reflect multiple episodes of dissolution and precipitation for two reasons: first, xenotime is extremely resistant to Pb loss in most circumstances (Cherniak, 2006), and particularly under low-grade conditions like those at Mount Tom Price, and, second, many of the populations coincide with established tectonothermal events.

There is little overlap between the populations documented by Rasmussen et al. (2007a) in the Mount Tom Price orebody and those in the Goldsworthy and Shay Gap belts, other than for the population at c. 1670 Ma. In particular, xenotime growth in the Shay Gap 7, Y2/3 and Sunrise Hill 1 ore bodies began up to c. 100 myr before the first documented growth event at Mount Tom Price. Although the c. 1000 Ma event at Goldsworthy and Nimingarra F has no counterpart in the xenotime data from Mount Tom Price, there is evidence in the deposit for monazite growth at c. 940 Ma (Rasmussen et al., 2007a).

9.3. Relationship to regional tectonothermal events

The history of Proterozoic deformation and metamorphism in granite–greenstone terrains of the Pilbara Craton is almost entirely unknown because of both an absence of Proterozoic successions on the craton to bracket offset along faults and shear zones, and the low-grade nature of the events means they have not left a zircon fingerprint. However, in situ dating of monazite and xenotime in low-grade metasedimentary rocks across the Pilbara Craton and farther south has established a broad framework of the cryptic tectonothermal events that have affected the craton (Fig. 21). Apart from a population of monazite at 2883 ± 6 Ma from the Strelley area, near the Abydos mine (Fig. 1), which is possibly related to reactivation of N- to NE-striking faults (Rasmussen et al., 2007b), most monazite has yielded dates between 2215 and 2145 Ma. Overall, monazite dates systematically young to the north, which is interpreted to reflect northward-propagation of the Ophthalmia fold-and-thrust belt from the southern margin of the craton (Rasmussen et al., 2005). The other population present in the samples from near Abydos is at 1652 ± 10 Ma (Rasmussen et al., 2007b), which coincides with 1680–1620 Ma medium- to high-pressure metamorphism and deformation of the Mangaroon Orogeny (Fig. 21) much farther south in the Capricorn Orogen (Sheppard et al., 2005) and shear zone reactivation over a wide area of the orogen (Sheppard et al., 2006).

The Hamersley Province was intruded by dolerite sills at c. 2210 Ma and by dolerite dykes at c. 2008 Ma (Müller et al., 2005); the former are interpreted to be the only preserved rock-record of a c. 2215 Ma large-igneous province (Krapež et al., 2017). Mesoproterozoic sedimentary rocks of the Eel Creek Formation that unconformably overlie the Shay Gap belt (Sheppard et al., 2016) were intruded by dolerite sills at c. 1070 Ma (Rasmussen et al., 2012; Wingate et al., 2012).

Duuring et al. (2016) documented magnetite formation related to faults and shear zones active during the c. 2955–2920 Ma North Pilbara Orogeny in deposits farther to the west and south. The oldest iron oxide mineral in the ore deposits of the Shay Gap and Goldsworthy belts is magnetite but no xenotime or monazite was identified intergrown with or included within magnetite, so its age of formation is unclear. We tentatively suggest that magnetite in the Shay Gap and Goldsworthy belts also formed during either the c. 3070 Ma Prinsep Orogeny or North Pilbara Orogeny, or both (Fig. 21).

The oldest phosphate growth event in the hematite ores from the Shay Gap belt (other than the single xenotime analysis at 2458 ± 11 Ma in Sample 281106-8) is recorded by a date of 2249 ± 19 Ma for xenotime from the Y2/3 pit (Sample 281106-8)

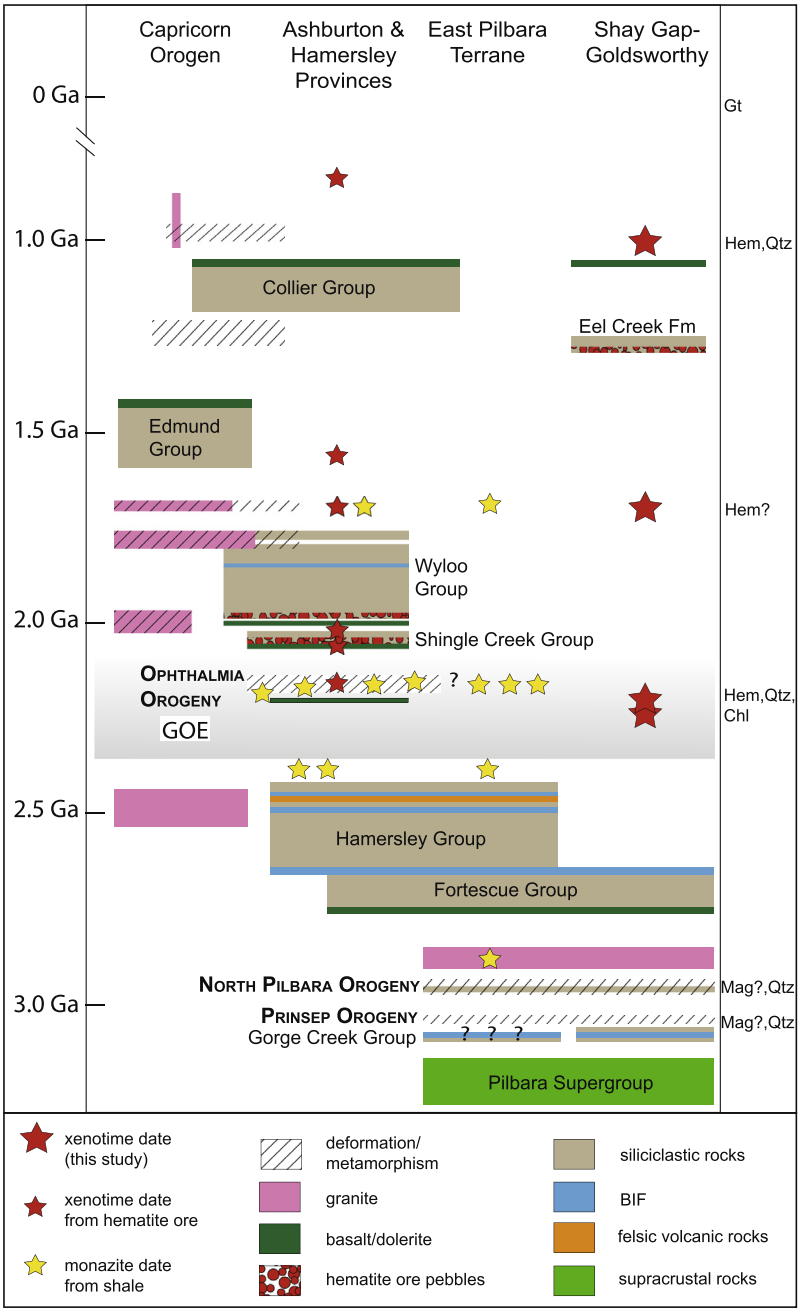

Fig. 21. Simplified time-space plot for the East Pilbara Terrane (with the Shay Gap belt shown separately), and the Capricorn Orogen and Ashburton and Hamersley Provinces to the south. Note the coincidence of monazite and xenotime ages from iron-ore deposits and shales in the East Pilbara Terrane and Ashburton and Hamersley provinces with orogenic events independently established farther south. Uncertainties on individual dates are smaller than the symbols. Ages of rock packages and orogenic events compiled from data in Blake et al. (2004), Trendall et al. (2004), Müller et al. (2005), Rasmussen et al. (2005), Sheppard et al. (2010), van Kranendonk et al. (2007), Krapež et al. (2015), Hickman (2016), Sheppard et al. (2017) and Krapež et al. (2017). The age for the Great Oxidation Event (GOE) is from Johnson et al. (2014), Lyons et al. (2014) and Luo et al. (2016). Monazite and xenotime geochronology data from Rasmussen et al. (2005, 2007a,b).

and a date of 2243 ± 31 Ma for xenotime in the Shay Gap 7 pit (Sample 291106-5). This event is associated with chlorite alteration of dolerite and hematite mineralisation. A single, imprecise monazite date of 2246 ± 48 Ma (1σ; Sample 160908-2) is only just within uncertainty of the oldest monazite dates for the 2210–2145 Ma Ophthalmia Orogeny (Rasmussen et al., 2005), but the two xenotime dates from Shay Gap 7 and Y2/3 are slightly older. The second growth event at c. 2180 Ma identified in Y2/3 and Sunrise Hill 1 (samples 281106-8 and 230608-1) is coeval with the Ophthalmia Orogeny, although the event is out of sequence given that the oldest ages for the orogeny are from the south and progressively young northwards (Rasmussen et al., 2005). It is possible that c. 2180 Ma xenotime growth records reactivation of Archean basement faults in the foreland distant from the developing Ophthalmia Fold Belt to the south. Reactivation of such structures has been documented in Cenozoic fold-and-thrust belts (e.g., Marshak et al., 2000; Ahmadhadi et al., 2007). However, our field work indicates that there is no evidence of thrusting or folding in the Shay Gap or Goldsworthy belts associated with ore formation.

Xenotime and monazite growth at c. 2250 Ma in the Shay Gap belt is also slightly older than c. 2210 Ma dolerite sills in the Hamersley Province dated by Müller et al. (2005). These authors attributed iron mineralisation in the Hamersley deposits to a suite of c. 2008 Ma dolerite dykes, but this thermal event is conspicuously absent in our dating of the Shay Gap and Goldsworthy belts. The fluidal nature of the DS4 dolerite dykes in the pits on the Nimingarra to Yarrie line, and their common occurrence as lows between swells on fault planes is consistent with a syn-ore age for the dykes. Unfortunately, attempts to date the DS4 dykes were unsuccessful. The fault array in the Shay Gap belt comprises NE-trending faults with sinistral oblique-slip and SE-trending faults with dextral normal oblique-slip. To generate these movements simultaneously on the two sets of structures requires almost east–west regional extension. Such extension could be responsible for the horst and gräben structures present in some of the pits.

Xenotime growth at c. 1670 Ma, and possible crystallisation of hematite, in the Sunrise Hill 1 pit coincides with the 1680–1620 Ma Mangaroon Orogeny within the Capricorn Orogen much farther south (Sheppard et al., 2005). As with monazite growth near Abydos (Fig. 1), xenotime growth at Sunrise Hill 1 may be related to reactivation of, and hydrothermal fluid flow channelled along, N- to NE-trending faults (see Rasmussen et al., 2007b) originally formed during the Mesoarchean (e.g., Krapež and Barley, 1987; Zegers et al., 1998) that were reactivated during volcanism and deposition of the 2775–2630 Ma Fortescue Group (Blake, 1993). There is also evidence from the eastern margin of the Pilbara Craton that reactivation of these faults was associated with Mn mineralisation during the Mesoproterozoic (Blake et al., 2011).

The youngest xenotime growth event recorded in the Goldsworthy and Shay Gap belts at c. 1000 Ma is associated with crystallisation of coarse-grained hematite and quartz in cavities. This event cannot be related to any documented tectonothermal events in the northeastern part of the Pilbara Craton. However, it is possible that this hydrothermal event was responsible for upgrading of c. 1300 Ma ore pebble conglomerates in the Y10 pit (Sheppard et al., 2017). In the Goldsworthy pit, xenotime dated at c. 1000 Ma is related to brecciation of the ore, suggesting that monazite growth was associated with brittle faulting on discrete structures. This deformation may have been driven by the 1030–950 Ma Edmundian Orogeny (Fig. 21) which was associated with widespread folding of cover rocks and shear zone reactivation in basement rocks farther south in the Capricorn Orogen (Sheppard et al., 2007; Occhipinti and Reddy, 2009).

It appears that all episodes of iron-ore formation along the northeastern margin of the Pilbara Craton may relate to far-field tectonic events, and are focused in what may have been long-lived brittle structures.

9.4. Hematite mineralisation and the timing of the Great Oxidation Event

The Nimingarra Iron Formation, which hosts high-grade hematite ore bodies in the Yarrie-Goldsworthy greenstone belts, was deposited at c. 3105 Ma (Sheppard et al., 2017). Our results suggest that hematite mineralisation began at c. 2250 Ma, more than 800 myr after deposition of the BIF. The formation of hematite ore from precursor iron-rich lithologies such as BIF and dolerite, requires large fluid-to-rock ratios and a major flux of oxidising fluids. The atmosphere lacked molecular oxygen until c. 2350 Ma, which marks the loss of mass independent fractionation of sulphur and the start of the Great Oxidation Event (GOE) (Bekker et al., 2004; Lyons et al., 2014; Luo et al., 2016). Prior to the GOE, redox sensitive detrital minerals such as pyrite, siderite and uraninite were stable in the atmosphere (Rasmussen and Buick, 1999; Johnson et al., 2014). After the start of the GOE, these minerals disappear coincident with the first appearance of red beds and iron oxide-rich palaeosols (Bekker et al., 2004; Johnson et al., 2014; Lyons et al., 2014), which record the oxidation of ferrous iron-bearing minerals.

Hydrothermal xenotime and monazite from the high-grade hematite ore bodies in the North Pilbara Craton indicate that hematite growth commenced at c. 2250 Ma, about 100 myr before the earliest generation of hydrothermal xenotime in the giant high-grade hematite ore in Mount Tom Price, Hamersley Province (Rasmussen et al., 2007a,b). Hematite mineralisation on the southern and northern margins of the Pilbara Craton commenced >100 myr after the start of the GOE. These findings suggest that high-grade hematite ore bodies are temporally related to the oxygenation of the atmosphere and Earth's land surface. Only after molecular oxygen accumulated in the atmosphere and terrestrial hydrosphere did widespread hematite growth commence. Palaeomagnetic studies (Schmidt and Clark, 1994) indicate that Hamersley Group BIFs experienced widespread hematite growth during or after the Ophthalmian Orogeny (2210–2145 Ma: Rasmussen et al., 2005). This is supported by high-resolution microscopy that shows that hematite dust in Hamersley Group BIFs is not a primary precipitate, but formed via post-depositional dissolution and oxidation of ferrous silicate nanoparticles (Rasmussen et al., 2014; Rasmussen et al., 2016a).

10. Conclusions

Hematite ore bodies in the Shay Gap and Goldsworthy belts formed where faults and dykes crossing at oblique angles to bedding focused hydrothermal fluids into BIF of the Nimingarra Iron Formation. On the Nimingarra line, where the strata strike N to NE, faults and dykes intersect bedding at a low angle, deposits plunge along the intersection and have considerable strike extent. Similarly, along the Shay Gap line, the controlling faults and primary layering both strike SE, so that most pits have significant strike extent. In contrast, at Sunrise Hill 3, strata strike SE and are cut by NE-trending faults and dolerite dykes which, although they provided a fluid pathway, served to limit the strike extent of mineralisation. However, it is not strike alone that determines the size of an ore deposit, but also the dip of the controlling fault relative to the dip of primary layering. The most favourable relationship is where the dip of the controlling fault and the dip of primary layering are nearly parallel, so that deposits have a long strike extent and great plunge depth (e.g., deposits on the Sunrise

Hill–Shay Gap line). The only lithological control on ore genesis is that the prospective host rocks are iron rich, regardless of whether they are BIF or dolerite. A substantial amount of ore in the Shay Gap belt was formed in dolerite dykes, because they too were iron-rich and chemically reactive.

Xenotime and monazite are present in trace amounts in some hematite-rich ore samples but the small size of many of the phosphate minerals, their low-U nature, and the presence of abundant common Pb in some samples combine to present a formidable challenge to U–Pb geochronology. Nevertheless, the SHRIMP U–Pb dating of hydrothermal xenotime and monazite presented here has provided the first absolute age determinations for iron mineralisation in the Algoma-type BIFs of the Pilbara Craton. Although some of the 'dates' cannot yet be considered populations owing to the small number of analytical spots, our results provide the first step towards integrating iron mineralisation with regional tectonothermal events.

Despite the difference in the ages of the BIFs in the Shay Gap and Goldsworthy belts (Mesoarchean) and those in the Hamersley Province (Neoarchean–Paleoproterozoic), in situ phosphate geochronology shows that iron mineralisation in both terrains is characterised by multiple episodes of xenotime growth (and by extension, hematite crystallisation) during the Proterozoic (cf. Rasmussen et al., 2007a). Furthermore, the age populations in both sets of iron deposits are not random, but can be related to independently established tectonothermal events (Fig. 21). A similar conclusion was reached by Rasmussen et al. (2016a,b) in their study of the Paleoproterozoic hematite iron-ores of the Marquette Range, in Michigan. The origin of the initial iron mineralisation in the Pilbara Craton is not clear, but could be related to coeval mafic magmatism during the Paleoproterozoic, with enrichment or remobilisation of hematite during several Proterozoic orogenic events centred farther south. Other iron deposits in Algoma-type BIF in the central part of the Pilbara Craton (Duuring et al., 2016), SW of the deposits studied here, may also have originated at the same time, being located along the NE-trending array of Archean fundamental structures (Fig. 1). It is possible that hematite mineralisation across the Pilbara Craton, from the Hamersley Province in the southwest to the Shay Gap belt in the northeast, are related to craton-scale fluid flow driven by multiple hydrothermal events related to mafic magmatism and orogenic activity.

The faults and dykes associated with mineralisation mark deep plumbing conduits, which may have focused the mixing of crustal or supracrustal iron-bearing fluids with oxygen-bearing meteoric fluids to thereby produce hematite-only ore bodies. It is probably no coincidence that all the recorded hydrothermal events in the deposits of the Shay Gap and Goldsworthy belts are all younger than, or close to the maximum age of the GOE, the significance being that meteoric fluids containing oxygen did not exist prior to then.

Acknowledgements

This work was supported by Australian Research Council (ARC) Linkage Grant LP0883956 to BR and BK. We thank Regina Malloy, Jack Richardson, Ilmar Tehnas and Adam Webb for their field and logistical support. Uranium–lead measurements were conducted using the SHRIMP at the John de Laeter Centre of Isotope Research at Curtin University. We thank Paul Duuring and an anonymous reviewer for helping to improve the final manuscript.

References

Ahmadhadi, F., Lacombe, O., Daniel, J.-M., 2007. Early reactivation of basement faults in Central Zagros (SW Iran): evidence from pre-folding fracture populations in Asmari Formation and Lower Tertiary Paleogeography. In: Lacombe, O., Roure, F., Lavé, J., Vergés, J. (Eds.), Thrust Belts and Foreland Basins: From Fold Kinematics to Hydrocarbon Systems. Springer, Berlin Heidelberg, Berlin, Heidelberg, pp. 205–228.

Angerer, T., Duuring, P., Hagemann, S.G., Thorne, W.S., McCuaig, T.C., 2014. A mineral system approach to iron ore in Archaean and Palaeoproterozoic BIF of Western Australia, In: Jenkin, G.R.T., Lusty, P.A.J., McDonald, I., Smith, M.P., Boyce, A.J., Wilkinson, J.J. (Eds.), Ore Deposits in an Evolving Earth. Geological Society, London, Special Publications 393, London, pp. 81–115.

Barley, M.E., Pickard, A.L., Hagemann, S.G., Folkert, S.L., 1999. Hydrothermal origin for the 2 billion year old Mount Tom Price giant iron ore deposit, Hamersley Province, Western Australia. Miner. Deposita 34, 784–789.

Bekker, A., Holland, H., Wang, P., Rumble III, D., 2004. Dating the rise of atmospheric oxygen. Nature 427, 117–120.

Blake, T.S., 1993. Archaean and early proterozoic geology of the Pilbara region, Western Australia Late Archaean crustal extension, sedimentary basin formation, flood basalt volcanism and continental rifting: the Nullagine and Mount Jope Supersequences, Western Australia. Precambr. Res. 60, 185–241.

Blake, T.S., Buick, R., Brown, S.J.A., Barley, M.E., 2004. Geochronology of a Late Archaean flood basalt province in the Pilbara Craton, Australia: constraints on basin evolution, volcanic and sedimentary accumulation, and continental drift rates. Precambr. Res. 133, 143–173.

Blake, T.S., Rothery, E., Muhling, J.R., Drake-Brockman, J.A.P., Sprigg, L.C., Ho, S.E., Rasmussen, B., Fletcher, I.R., 2011. Two episodes of regional-scale Precambrian hydrothermal alteration in the eastern Pilbara, Western Australia. Precambr. Res. 188, 73–103.

Brandt, R.T., 1966. The genesis of the Mount Goldsworthy iron ore deposits of northwest Australia. Econ. Geol. 61, 999–1009.

Bühler B., 2008. Stratigraphy of the Archaean Shay Gap greenstone belt, Pilbara Craton, Western Australia. (MSc Thesis). Albert-Ludwigs-Universität, Freiburg, 124p.

Cherniak, D.J., 2006. Pb and rare earth element diffusion in xenotime. Lithos 88, 1–14.

Dawes, P.R., Smithies, R.H., Centofanti, J., Podmore, D.C., 1995a. Sunrise Hill unconformity: a newly discovered regional hiatus between Archaean granites and greenstones in the northeastern Pilbara Craton. Aust. J. Earth Sci. 42, 635–639.

Dawes, P.R., Smithies, R.H., Centofanti, J., Podmore, D.C., 1995b. Unconformable contact relationships between the Muccan and Warrawagine batholiths and the Archaean Gorge Creek Group in the Yarrie mine area, northeastern Pilbara. Geol. Surv. West. Aust., 23p Record 1994/3.

Duuring, P., Teitler, Y., Hagemann, S.G., Angerer, T., 2016. MRIWA report project M426: exploration targeting for BIF-hosted Fe deposits in the Pilbara Craton, Western Australia. Geol. Surv. West. Aust., 263p Report 163.

Eriksson, K.A., Krapež, B., Fralick, P.W., 1994. Sedimentology of Archean greenstone belts: Signatures of tectonic evolution. Earth-Sci. Rev. 37, 1–88.

Ferguson, K.M., Ruddock, I., 2001. Mineral occurrences and exploration potential of the east Pilbara. Geol. Surv. West. Aust., 114p Report 81.

Figueiredo e Silva, R.C., Lobato, L.M., Rosière, C., Hagemann, S., Zucchetti, M., Baars, F., Morais, R., Andrade, I., 2008. A hydrothermal origin for the jaspilite-hosted, giant Serra Norte iron ore deposits in the Carajas mineral province, Para state, Brazil, In: Hagemann, S.G., Rosière, C.A., Gutzmer, J., Beukes, N. (Eds.), Banded Iron Formation-Related High-Grade Iron Ore. Society of Economic Geologists Inc, pp. 255–290.

Fletcher, I.R., McNaughton, N.J., Aleinikoff, J.A., Rasmussen, B., Kamo, S.L., 2004. Improved calibration procedures and new standards for U-Pb and Th–Pb dating of Phanerozoic xenotime by ion microprobe. Chem. Geol. 209, 295–314.

Fletcher, I.R., McNaughton, N.J., Davis, W.J., Rasmussen, B., 2010. Matrix effects and calibration limitations in ion probe U-Pb and Th–Pb dating of monazite. Chem. Geol. 270, 31–44.

Hickman, A.H., 1983. Geology of the Pilbara Block and its environs. Geol. Surv. West. Aust., 268p Bulletin 127.

Hickman, A.H., 1990. Geology of the Pilbara craton, In: Ho, S.E., Glover, J.E., Myers, J. S., Muhling, J.R. (Eds.), Third International Archaean Symposium, Excursion Guidebook, University of Western Australia, Geology Department and University Extension, Publication 21, pp. 1–13.

Hickman, A.H., 2016. Northwest Pilbara Craton: a record of 450 million years in the growth of Archean continental crust. Geol. Surv. West. Aust., 104p Report 160.

Hickman, A.H., Smithies, R.H., Tyler, I.M., 2010. Evolution of active plate margins: West Pilbara Superterrane, De Grey Superbasin, and Fortescue and Hamersley Basins – a field guide. Geol. Surv. West. Aust. 2010, 1–74. Record 2010/3.

Huston, D.L., Sun, S.-S., Blewett, R., Hickman, A.H., Van Kranendonk, M.J., Phillips, D., Baker, D., Brauhart, C., 2002. The timing of mineralization in the Archean North Pilbara Terrain, Western Australia. Econ. Geol. 97, 733–755.

Johnson, J.E., Gerpheide, A., Lamb, M.P., Fischer, W.W., 2014. O2 constraints from Paleoproterozoic detrital pyrite and uraninite. Geol. Soc. Am. Bull. 126, 813–830.

Krapež, B., 1989. Depositional styles and geotectonic settings of Archaean metasedimentary sequences: evidence from the Lalla Rookh Basin, Pilbara Block, Western Australia. Ph.D. thesis, The University of Western Australia (unpublished).

Krapež, B., 1993. Sequence stratigraphy of the Archaean supracrustal belts of the Pilbara Block, Western Australia. Precambr. Res. 60, 1–45.

Krapež, B., Müller, S.G., Fletcher, I.R., Rasmussen, B., 2017. A tale of two basins? Stratigraphy and detrital zircon provenance of the Palaeoproterozoic Turee Creek and Horseshoe basins of Western Australia. Precambr. Res. 294, 67–90.

Krapež, B., Barley, M.E., 1987. Archaean strike-slip faulting and related ensialic basins: evidence from the Pilbara Block, Australia. Geol. Mag. 124, 555–567.
Krapež, B., Eisenlohr, B., 1998. Tectonic settings of Archaean (3325–2775 Ma) crustal-supracrustal belts in the West Pilbara Block. Precambr Res. 88, 173–205.
Krapež, B., Müller, S.G., Bekker, A., 2015. Stratigraphy of the Late Palaeoproterozoic (~2.03 Ga) Wooly Dolomite, Ashburton Province, Western Australia: a carbonate platform developed in a failed rift basin. Precambr. Res. 271, 1–19.
Lewis, J.D., Rosman, K.J.R., de Laeter, J.R., 1975. The age and metamorphic effects of the Black Range dolerite dyke. Geol. Surv. West. Aust., 80–88 Annual Report 1974.
Ludwig, K.R., 2009. Squid 2; a user's manual (revised 12th April, 2009). Berkeley Geochronology Center Special Publication 5, p. 104.
Luo, G., Ono, S., Beukes, N.J., Wang, D.T., Xie, S., Summons, R.E., 2016. Rapid oxygenation of Earth's atmosphere 2.33 billion years ago. Sci. Adv. 2, e1600134.
Lyons, T.W., Reinhard, C.T., Planavsky, N.J., 2014. The rise of oxygen in Earth/'s early ocean and atmosphere. Nature 506, 307–315.
MacLeod, W.N., 1966. The geology and iron deposits of the Hamersley Range area, Western Australia. Geol. Surv. West. Aust., 170p Bulletin 117.
Marshak, S., Karlstrom, K., Timmons, J.M., 2000. Inversion of Proterozoic extensional faults: an explanation for the pattern of Laramide and Ancestral Rockies intracratonic deformation, United States. Geology 28, 735–738.
Martin, D.M., Li, Z.X., Nemchin, A.A., Powell, C.M., 1998. A pre-2.2 Ga age for giant hematite ores of the Hamersley Province, Australia? Econ. Geol. 93, 1084–1090.
Morris, R.C., 1980. A textural and mineralogical study of the relationship of iron ore to banded iron-formation in the Hamersley iron province of Western Australia. Econ. Geol. 75, 184–209.
Morris, R.C., 1985. Genesis of iron ore in banded iron-formation by supergene and supergene-metamorphic processes: a conceptual model. In: Wolf, K.H. (Ed.), Handbook of Strata-Bound and Stratiform Ore Deposits, vol. 13. Elsevier, Amsterdam, pp. 73–235.
Müller, S.G., Krapež, B., Barley, M.E., Fletcher, I.R., 2005. Giant iron-ore deposits of the Hamersley province related to the breakup of Paleoproterozoic Australia: New insights from in situ SHRIMP dating of baddeleyite from mafic intrusions. Geology 33, 577–580.
Occhipinti, S.A., Reddy, S.M., 2009. Neoproterozoic reworking of the Palaeoproterozoic Capricorn Orogen of Western Australia and implications for the amalgamation of Rodinia. Geol. Soc., London, Spl. Publ. 327, 445–456.
Podmore, D.C., 1990. Shay Gap-Sunrise Hill and Nimingarra iron ore deposits. In: Hughes, F.E. (Ed.), Geology of the Mineral Deposits of Australia and Papua New Guinea. The Australasian Institute of Mining and Metallurgy, Melbourne, pp. 137–140.
Powell, C.M., Oliver, N.H.S., Li, Z.-X., Martin, D.M., Ronaszeki, J., 1999. Synorogenic hydrothermal origin for giant Hamersley iron oxide ore bodies. Geology 27, 175–178.
Rasmussen, B., Buick, R., 1999. Redox state of the Archean atmosphere: Evidence from detrital heavy minerals in ca. 3250–2750 Ma sandstones from the Pilbara Craton, Australia. Geology 27, 115–118.
Rasmussen, B., Fletcher, I.R., Gregory, C.J., Muhling, J.R., Suvorova, A.A., 2012. Tranquillityite: the last lunar mineral comes down to Earth. Geology 40, 83–86.
Rasmussen, B., Fletcher, I.R., Muhling, J.R., 2007a. In situ U-Pb dating and element mapping of three generations of monazite: Unravelling cryptic tectonothermal events in low-grade terranes. Geochim. Cosmochim. Acta 71, 670–690.
Rasmussen, B., Fletcher, I.R., Muhling, J.R., Thorne, W.S., Broadbent, G.C., 2007b. Prolonged history of episodic fluid flow in giant hematite ore bodies: evidence from in situ U-Pb geochronology of hydrothermal xenotime. Earth Planet. Sci. Lett. 258, 249–259.
Rasmussen, B., Fletcher, I.R., Sheppard, S., 2005. Isotopic dating of the migration of a low-grade metamorphic front during orogenesis. Geology 33, 773–776.
Rasmussen, B., Krapež, B., Meier, D.B., 2014. Replacement origin for hematite in 2.5 Ga banded iron formation: Evidence for postdepositional oxidation of iron-bearing minerals. Geological Society of America Bulletin 126, 438–446.
Rasmussen, B., Muhling, J.R., Suvorova, A., Krapež, B., 2016a. Dust to dust: evidence for the formation of "primary" hematite dust in banded iron formations via oxidation of iron silicate nanoparticles. Precambr. Res. 284, 49–63.
Rasmussen, B., Zi, J.-W., Sheppard, S., Krapež, B., Muhling, J.R., 2016b. Multiple episodes of hematite mineralization indicated by U-Pb dating of iron-ore deposits, Marquette Range, Michigan, USA. Geology 44, 547–550.
Schmidt, P.W., Clark, D.A., 1994. Palaeomagnetism and magnetic anisotropy of Proterozoic banded-iron formations and iron ores of the Hamersley Basin, Western Australia. Precambr. Res. 69, 133–155.
Sheppard, S., Farrell, T.R., Bodorkos, S., Hollingsworth, D., Tyler, I.M., Pirajno, F., 2006. Late Paleoproterozoic (1680–1620 Ma) sedimentation, magmatism and tectonism in the Capricorn Orogen. Geol. Surv. West. Aust., 11–12 Record 2006/3.
Sheppard, S., Johnson, S.P., Wingate, M.T.D., Kirkland, C.L., Pirajno, F., 2010. Explanatory Notes for the Gascoyne Province. Geological Survey of Western Australia, 336p.
Sheppard, S., Rasmussen, B., Muhling, J.R., Farrell, T.R., Fletcher, I.R., 2007. Grenvillian-aged orogenesis in the Palaeoproterozoic Gascoyne Complex, Western Australia: 1030–950 Ma reworking of the Proterozoic Capricorn Orogen. J Metamorph Geol. 25, 477–494.
Sheppard, S., Krapež, B., Zi, J.-W., Rasmussen, B., Fletcher, I., 2016. The 1320 Ma intracontinental Wongawobbin Basin, Pilbara, Western Australia: a far-field response to Albany–Fraser–Musgrave tectonics. Precambr. Res. 285, 58–79.
Sheppard, S., Krapež, B., Zi, J.-W., Rasmussen, B., Fletcher, I.R., 2017. SHRIMP U-Pb zircon geochronology establishes that banded iron formations are not chronostratigraphic markers across Archean greenstone belts of the Pilbara Craton. Precambr. Res. 292, 290–304.
Sheppard, S., Occhipinti, S.A., Nelson, D.R., 2005. Intracontinental reworking in the Capricorn Orogen, Western Australia: the 1680–1620 Ma Mangaroon Orogeny*. Aust. J. Earth Sci. 52, 443–460.
Smithies, R.H., 2004. Geology of the De Grey and Pardoo 1:100 000 sheets. Geological Survey of Western Australia, 1:100 000 Geological Series Explanatory Notes, 24p.
Stacey, J.S., Kramers, J.D., 1975. Approximation of terrestrial lead isotope evolution by a two-stage model. Earth Planet. Sci. Lett. 26, 207–221.
Taylor, D., Dalstra, H.J., Harding, A.E., Broadbent, G.C., Barley, M.E., 2001. Genesis of high-grade hematite orebodies of the Hamersley Province, Western Australia. Econ. Geol. 96, 837–873.
Teitler, Y., Duuring, P., Hagemann, S.G., 2017. Genesis history of iron ore from Mesoarchean BIF at the Wodgina mine, Western Australia. Aust. J. Earth Sci., 1–22
Thorne, A.M., Trendall, A.F., 2001. Geology of the Fortescue Group, Pilbara Craton, Western Australia. Geol. Surv. West. Aust., 249p Bulletin 144.
Trendall, A.F., Compston, W., Nelson, D.R., De Laeter, J.R., Bennett, V.C., 2004. SHRIMP zircon ages constraining the depositional chronology of the Hamersley Group, Western Australia. Aust. J. Earth Sci. 51, 621–644.
Tyler, I.M., 1991. The geology of the Sylvania Inlier and the southeast Hamersley Basin. Geol. Surv. West. Aust. 138, 108p.
Van Kranendonk, M.J., Hickman, A.H., Smithies, R.H., Williams, I.R., Bagas, L., Farrell, T.R., 2006. Revised lithostratigraphy of Archean supracrustal and intrusive rocks in the northern Pilbara Craton, Western Australia. Geol. Surv. West. Aust. 2006 (15), 57p.
Van Kranendonk, M.J., Smithies, R.H., Hickman, A.H., Champion, D.C., 2007. Review: secular tectonic evolution of Archean continental crust: interplay between horizontal and vertical processes in the formation of the Pilbara Craton, Australia. Terra Nova 19, 1–38.
Waters, P.J., 1998. Geology of the Y2/3 and Y10 iron-ore deposits, Yarrie, Western Australia, In: Berkman, D.A., MacKenzie, D.H. (Eds.), Geology of Australian and Papua New Guinean mineral deposits. Australasian Institute of Mining and Metallurgy, Monograph 22, pp. 371–374.
Williams, I.R., 1999. Geology of the Muccan 1:100 000 sheet. Geological Survey of Western Australia, 1:100 000 Geological Series Explanatory Notes, 39p.
Williams, I.R., 2000. Geology of the Cooragoora 1:100 000 sheet. Geological Survey of Western Australia, 1:100 000 Geological Series Explanatory Notes, 23p.
Williams, I.R., 2003. Yarrie, W.A. (3rd edition). Geological Survey of Western Australia, 1:250 000 Geological Series Explanatory Notes, 84p.
Wingate, M.T.D., 1999. Ion microprobe baddeleyite and zircon ages for Late Archaean mafic dykes of the Pilbara Craton, Western Australia. Aust. J. Earth Sci. 46, 493–500.
Wingate, M.T.D., Kirkland, C.L., Hickman, A.H., Williams, I.R., 2012. 178187: dolerite sill, Reid Bore. Geochronology Record 1084: Geological Survey of Western Australia.
Zegers, T.E., de Keijzer, M., Passchier, C.W., White, S.H., 1998. The Mulgandinnah Shear Zone; an Archean crustal scale strike-slip zone, eastern Pilbara, Western Australia. Precambr. Res. 88, 233–247.